Multimodal analysis of immune cell heterogeneity around implanted biosynthetic scaffold in large-area wound healing

Yang Yang[a#], Chenyu Chu[a#], Chen Hu[a], Chenbing Wang[a],

Yili Qu[a*], Yi Man[a*]

[a] Department of Oral Implantology &State Key Laboratory of Oral Diseases & National Clinical Research Center for Oral Diseases, West China Hospital of Stomatology, Sichuan University, Chengdu 610041, China.

 # These authors contributed equally to this work

** Corresponding to Yi Man, E-mail: manyi780203@126.com and Yili Qu, E-mail: qqyili@126.com*

Corresponding author:

Yi Man, DDS, Ph.D

Professor and Chair

Department of Oral Implantology, West China Hospital of Stomatology, Sichuan University, 14#, 3rd section, Renmin South Road

Chengdu 610041, China

Tel: 0086-28-85503571

E-mail: manyi780203@126.com

Yili Qu, DDS, Ph.D

Associate Professor

State Key Laboratory of Oral Diseases, West China Hospital of Stomatology, Sichuan University, 14#, 3rd section, Renmin South Road

Chengdu 610041, China

Tel: 0086-28-85503571

E-mail: qqyili@126.com

Abstract

Fibrotic scar devoid of skin appendages bring great challenge to tissue engineering, particularly in severe large area wound. Intriguingly, HF (hair follicle) can regenerate specifically in the large wound center of adult mice, termed wound-induced hair follicle neogenesis (WIHN). Single-cell RNA sequencing (scRNA-seq) comparison of wound in different size showed increased activation of adaptive immune systems along with predominance of HF precursor cells in large wound. Integration the gene expression profiles of spatial transcriptomic (ST) and scRNA-seq highlighted the preferential aggregation of T cells, pro-inflammatory macrophage (PIM) and monocyte in the margin and center of large wound co-localizing with HF precursor cells. Local pro-regenerative immune response among them provided potential therapeutic target for the further HF regeneration. Aligned electrospinning scaffolds were previously shown to accelerate small wound healing with the immunomodulatory effect of T cells and macrophages in small wound. Here we observed that wound recapitulated normal skin architecture with the implantation of biodegradable biosynthetic scaffold despite wound size. The scaffolds did not trigger a severe foreign body response (FBR) but showed the immunomodulatory effect on adaptive immune system. Enlarged distribution of the “pro-regenerative” immune niche overlapping with HF precursor cells may

account for the well-proportioned de novo HF in scaffold-implanted group. Collectively, our study illustrated that manipulating the adaptive immune system may stimulate de novo HF regeneration via local cell-cell interactions. And the easy-fabricating electrospinning membrane with appropriate biocompatibility also offered available treatment options in severe skin defect regeneration.

Keywords

Wound-induced hair follicle neogenesis, Immune microenvironment, Immunomodulatory, Tissue engineering, Single-cell RNA-Seq, Spatial transcriptomics.

Introduction

Following severe injury, skin wounds in adult generally heal by fibrotic scarring devoid of HF [1]. Large lifelong scar can seriously affect the patient's daily life, which is one of the primary impediments to skin wound healing[2]. Biosynthetic materials are one of the efficient treatments for severe wound of skin[3]. However, most scaffold materials are designed for small area wound which lacking appropriate biocompatibility, degradability, and ability to regenerate dermal appendages especially in large area skin wound[4].

Intriguingly, some capacity for “half-functional” regeneration has been demonstrated in large (larger than 1 cm^2) full thickness wound of adult mice skin in WIHN model[5,6]. It has been inferred that immune cells

(mainly macrophages, T cells) might be the key orchestrators of wound healing that selectively promoting scarring[7-9] or regenerative WIHN[10-13]. Nevertheless, the impact of immune system in response to wound is incompletely understood, and underlying mechanism that nascent HF restricting to the large wound center remains unclear neither. Unrevealing the spatiotemporal heterogeneity of immune cells between the scar or WIHN model might be a fascinating way to understand the mechanism of functional wound regeneration and thus provided therapeutic target for further treatment.

Along with deeper understanding of biological process and emergence of mature engineering techniques, there are growing possibility for well-designed biosynthetic materials to achieve specific therapeutic goals[14]. Biological cues can be integrated into polymer scaffold to create a mimic of the native extracellular matrix (ECM), which is the framework guiding the activity of immune cells [15,16]. Formation of a pro-regenerative immune microenvironment might support the development of proper functional skin regeneration instead of fibrotic scar[17]. Our previous study has showed that the aligned topography electrospinning scaffold was able to lead to an enhanced regeneration of HF (small wound, diameter 6mm), along with the immunomodulatory effect of activating the adaptive system[18]. On this basis, we next found that aligned scaffold with 300nm diameter has a better pro-regenerative effect (small wound,

diameter 6mm), along with the recruitment of reparative macrophages [19]. However, we wonder if ECM scaffold could exert the regenerative effect in mouse large wounds either.

To sum up, there still some elusive questions to be solved till now: (1) Spatial heterogeneity of immune-microenvironment between small wound, large wound margin, and large wound center;(2) Whether the biosynthetic ECM scaffold exerts the further pro-regenerative effect when implanted in the large wound, and the underlying immune-regulatory mechanism;(3) Is there still any difference between small or large wound healing with implanted scaffold? To answer the question above, here we integrated the high-dimensional multiomics approaches including bulk-tissue RNA sequencing (bulk-seq), scRNA-seq, and ST to delineate the delicate spatial characteristics of immune-microenvironment in different wound size with/without implanted scaffold. Multimodal analysis highlighted the preferential aggregation of T cells, PIM, and monocyte in the large wound center, as well as whole wound surrounding implanted ECM scaffold. Those immune cells were observed to co-localize with the HF precursor cells, which was required to initiate HF formation[20] . Abundant local intercellular communications between them predicted by Cellchat supported the therapeutic potential of adaptive immune system in functional tissue regeneration.

WIHN occurred in large wound center with activation of adaptive immune system

We respectively created full-thickness small wound (Ctrl_SW, diameter=0.6cm) and large wound (Ctrl_LW, diameter =1.5cm) in mice loose dorsal skin. To mimic the healing model of human's tight skin, silicone splints were sutured with the wound margin to minimize the contraction of mice's panniculus carnosus in response to wounding[21] (Fig. 1, A and B). Comparison of Ctrl_SW and Ctrl_LW group during the remodeling phase (day 28) confirmed that small wounds healing with the characteristic of fibrotic scar: excessive dense, parallel collagen deposition without dermal appendages. While de novo hair follicles could regenerate in large wound center, suggesting an "half-regenerative" micro-environment (Fig. 1C).

To ask whether this regenerative capacity correlated with immune response, we compared Ctrl_SW and Ctrl_LW groups for bulk-RNA transcription on POD7, a time point of both tissue proliferation and immune cell recruitment. In comparison with small wound, the large wound showed up-regulated gene expression in Gene Ontology (GO) terms including hair follicle development and αβT cell differentiation, and Kyoto Encyclopedia of Genes and Genomes (KEGG) pathways including Wnt signaling pathway and Th17 cell differentiation pathway (Fig. 1D). Volcano plots showed that genes related to adaptive immune

responses were significantly up regulated in Ctrl_LW group, including genes (Lef1, Shh) which had been convinced to be correlated with HF regeneration[22-24] (Fig. 1E). Correlation heatmap showed the positive correlation between HF regeneration related genes and adaptive immune response related genes among 6 samples (Fig. 1 F). Immunofluorescent (IF) and immunohistochemistry (IHC) staining for Cd3 confirmed that large wound center maintained substantial adaptive T cell infiltration on POD 7 (Fig. 1G).

ScRNA-seq revealed higher proportion of HF precursor cells from Ctrl_LW group

Next, we undertook scRNA-seq to compare the transcriptional profiling between Ctrl_SW and Ctrl_LW group at single-cell resolution (Fig. S1A). After quality control, 18,621 cell were included in the final dataset (11,217 from the Ctrl_LW group and 7,404 from the Ctrl_SW group). We firstly categorized the cells into 10 main clusters based on gene expression profiles using Seurat, and the proportion of cells from two groups were shown in Fig. S1B. Top (based on average |log2FC| value) marker genes for each cell cluster were shown in the Fig. S1C.

Firstly, we extracted cells defined as fibroblast and performed subcluster analysis (Fig. 2A) based on marker genes profiles published before[8,18,20,25-29] (Fig. 2B).Since dermal papilla (DP) cells ($Papp2^{+}Corin^{+}$)

belonged to the existing HF in normal skin adjacent to the wound, which was not the focus of this part. We next conducted in-depth analysis of wound fibroblasts and defined them as following categories: upper layer papillary fibroblast (PF) (Crabp1^{+}Fabp5^{+}), lower layer fibroblast including reticular fibroblasts (RF) (Dpp4^{+}Mgp^{+}Gpx3^{+}Plac8^{+}) & hypodermis lipo-fibroblast (LF) (Mfap4^{+} Cd34^{+}), as well as wound-activated myofibroblast (Acta2^{+}Tagln^{+}Mki67^{+}) and myeloid-derived adipocyte progenitors (Macf) (Pdgfra^{+} Lyz2^{+} Ptprc^{+} Plin2^{+}). The composition of fibroblast subclusters from each group (Fig. 2C) might explain the reason why small wound generally heal with scarring devoid of HFs. In accordance with previous report[20], the major initial wave of dermal repair in small wound is mediated by the lower lineage fibroblast including LF (49.88%) and RF (21.93%)(Fig. 2C), which is respectively related to hypodermis adipocytes formation and dermis collagen fibril organization (Fig. 2D).The predominance of RF and LF in small wound might be the main cause for the excessive collagen deposition[30]. In contrast, there were more upper lineage PF (36.11%) in large wound (Fig. 2C). The PF in this dataset consisted of 2 subclusters including PF1 (Runx1^{+}Inhba^{+})[25] and PF2 (Notch1^{+}Prdm1^{+})[31], both of which were believed to have the capacity to support HF initiation (Fig. 2D). Intriguingly, there were 134 Macf cells specifically exist in large wound, which had been proved to be the progenitors of adipocyte around neo-HF

in large wound center[26].

Next, we extracted cells assigned as keratinocyte and performed subcluster analysis. Known markers[10,18,28,32,33] were used to define keratinocyte subclusters identity (Fig. 2, E and G). Hair follicle stem cell (HFSC) ($Lgr5^{+}Lrig1^{+}$)[10] and HFP (hair follicle progenitor) ($Msx2^{+}Krt28^{+}Mki67^{+}$)[33] were believed to be the dominant epithelial contributor to the de novo HF. The proportion of HFP was higher in Ctrl_LW (12.97%) than Ctrl_SW (3.14%). Collectively, the higher proportion of HF precursor cells including PF (mesenchymal origin), HFSC and HFP (epithelial origin) may account for the initiation of WIHN specially in large wound. Besides, since the HF cycles through phases of growth (anagen), regression (catagen), and rest (telogen)[28]. Keratinocytes could be robustly assigned to two cell types: permanent part of the epidermis (interfollicular epidermis, sebaceous gland, and non-cycling portion of the HF) and keratinocytes from the cycling part of the anagen HF. The anagen HF cells in this dataset were composed of ($Ube2c^{+}Ccnb1^{+}$) germinative layer (GL) cells, ($Mt4^{+}$ $Rnaset2b^{+}Krt35^{+}$) medulla (MED) and cortex cells, and ($Krt25^{+}Krt27^{+}$) inner root sheath (IRS) layers cells. Since the C57/B6 mice were in their second telogen (postnatal days P46–70) on POD7.The higher proportion of anagen HF cells in Ctrl_LW suggested a stronger HF telogen–anagen transition (TAT) around the large wound as well.

More abundant monocytes/macrophages and more diverse heterogeneity of T cell from Ctrl_LW group

Macrophages are highly plastic immune cells upon different environment stimulators and contribute to most phases of tissue repair[34].They phagocytose pathogens or debris instantly in response to wounding. Then, they activate the adaptive immune system through specific antigen presentation, which is believed to bridge the innate and adaptive immune system[16].To explore the heterogeneity of macrophages, we extracted the monocyte and macrophages (MAC) and subjected them to further subcluster analysis. Canonical classification systems of macrophages including “classically activated” M1 macrophages and “alternatively activated” M2 macrophages were shown insufficiently to identify the phenotypes in this condition (Fig. 3B).Based on known markers[18], three subsets including $Ccl8^{+}$ $Folr2^{+}C1qa^{+}Mrc1^{+}$ anti-inflammatory macrophages (AIM), $Mmp12^{+}Arg1^{+}Inhba^{+}Nos2^{+}$ pro-inflammatory macrophages (PIM) and $Ly6c2^{+}Plac8^{+}Cytip^{+}H2\text{-}Eb1^{+}$ monocyte (Mono) were determined (Fig. 3, A and C). The pseudo-temporal trajectory of the three subsets revealed that monocytes developed into PIM firstly and then polarized into AIM (Fig. 3E). KEGG enrichment analysis revealed that Mono might play role in antigen presentation and T cell differentiation, and Mono in Ctrl_LW group specifically related to nature killer cell mediated cytotoxicity; PIM was

related to pro-inflammatory pathways, among which IL-17 pathway was up-regulated in Ctrl_LW group; AIM was correlated to lysosome, phagosome, and endocytosis which belonged to innate immune response (Fig. 3D).The higher proportion of all three macrophage subsets as well as neutrophil and dendritic cell in Ctrl_LW (Fig. S2) suggested there was a more complex environment both in innate immune response as well as the activation of adaptive system in large wound.

Recently, the role of adaptive immune cells on the formation of the pro-regenerative immune microenvironment has been stressed out[35]. Although the role of γδ T cells in facilitating WIHN [11,13] has been demonstrated, the relationship of adaptive immune cells with HF regeneration is largely unknown till now. The proportion of T cell was higher in Ctrl_LW group (Fig. S1B) in accordance with the result of bulk-seq and histological results. Based on published marker[18,36], T cells were clustered into seven subsets (Fig. 3, F and G) including Cd8b1^{+} cytotoxic T cell (CTL), Tyrobp^{+}Nkg7^{+}Xcl^{+} nature killer T cell1 (NKT1), Tyrobp^{+}Ccl2^{+} nature killer T cell2 (NKT2), Il17f^{+} T helper17 (Th17), Foxp3^{+} T regulatory cell (Treg), Trdv4^{+}Cd7^{+}Ctsw^{+} γδT cell1 (Tγδ1) and Cd7^{+}Ctsw^{+}Gnb21l^{+} γδT cell2 (Tγδ2). As shown in Fig. 3F, γδT cell was the only predominant subtype of T cell in Ctrl_SW (70.82%), which was related to endocytosis belonging to innate immune system (Fig 3H). In contrast, there were more abundant subtypes of adaptive αβT cells in

Ctrl_LW group, which were related to Th17 and Th1/Th2 cell differentiation (Fig. 3H). Besides, the proportion of Ccl2^{high} NKT2 cell was also higher in Ctrl_LW, which was related to the recruitment of inflammatory macrophage[37]. What's more, there were more Tregs in large wound which were believed to paly role in suppressing excessive collagen deposition and driving HFSC differentiation &migration[7]. To sum up, the diverse subtypes of T cell from Ctrl_LW group suggested a more active adaptive immune micro-environment in skin large wound.

Identification of single-cell heterogeneity through the integration of spatial transcriptomics and sc RNA-seq profiling

To further explore the spatial characteristic of above cells in wound center or wound edge, we applied the spatial transcriptomics to analyze spatial gene expression profiles of small and large wound on POD7 (Fig. 4A). The epidermal, dermal, hypodermal layers and granulation tissue of the wounds were easily delineated histologically (Fig. 4B). Different regions from each group could be clearly distinguished on uniform manifold approximation and projection (UMAP) plot (Fig. 4C). Representative genes for each region were shown in Fig. S3A. We could find the clear outline of neo-epidermis based on Krt6a expression (as well as other keratinocyte related genes) (Fig. S3B). Similarly, fibroblast activity was evaluated using marker genes such as Col1a1, which were most dominant in granulation tissue (Fig. S3B).

First, we extracted the epidermis and subjected it to the subcluster analysis (Fig. S4A). Based on published research[38,39], the repairing epidermis is organized into three regions: migration zone (migration-only), mixed zone (intermediate region of both proliferation and migration), and proliferation zone (proliferation-only region away from the wound) (Fig. S4, B and C).To overcome the low resolution of ST (one spot usually contains 1 to 10 cells), we integrated the ST and scRNA-seq gene expression profiles using Addmodulescore function in Seurat[40].The top50 differentially expressed marker genes (ranked by avg_log2FC value) of each keratinocytes subclusters from scRNA-seq(defined in Fig.2 E-F) were used to score each ST spots gene expression profiles. The predicted spatial distributions for our scRNA-seq clusters were able to be projected to each spot using SpatialFeaturePlot function. As shown in the Fig. 4D, although $Lgr5^+$ HFSC cells were less abundant in the neo-epithelium compared to $Lgr6^+$ IFE basal cells. HF-related HFSC cells were shown to contribute to the proliferation zone of epidermis exclusively in large wound.

Next, we extracted the granulation tissue and subjected it to the subcluster analysis. Unsupervised clustering categorized the granulation tissue into 13 clusters based on global gene expression patterns (Fig. S5 A-C). According to gene expression similarities, 13 unsupervised clusters were grouped into three functional clusters including small wound (SW),

upper layer of large wound (LW_upper) and lower layer of large wound (LW_lower) (Fig.S5D). GO analysis showed the LW_upper functional cluster (especially cluster LW_C1) was related to HF morphologies. Scoring spots in each section with fibroblast-signature genes from our scRNA-seq (defined in Fig.2 A-D) showed that the PF (HF-related) exhibit strong spatial preferences within the large wound upper layer (especially wound center). While lower lineage fibroblasts including RF and LF preferentially resided in the large wound lower layer. In contrast, there was not any obvious aggregation tendency of fibroblast subpopulations in small wounds (Fig.4 E).

It is noteworthy that lymphocyte chemotaxis and antigen presentation related genes were enriched in migrating epidermis as well as upper layer of large wound. In contrast, there were innate immune system related genes that enriched in small wound (Fig.S4 D and S5 E). To explore how distinct immune cell types may contribute to the healing procedure in different wound size, the expression of immune cell subclusters marker genes (defined in Fig.3) was surveyed. As shown in Fig.5 E, macrophages including AIM, PIM and Mono diffusely distributed in small wounds, while PIM (related to pro-inflammatory pathways) and Mono (related to antigen presentation) showed the preferentially aggregation in large wound center and wound margin. Besides, almost all T cell subclusters were exclusively expressed in large wound center and

wound margin. In contrast, there seem lack observable T cell infiltration in small wound.

To sum up, it was in large wound that we observed the preferential aggregation of HFSC in migrating epithelium, and PF in granulation tissue (especially upper layer center). What's more, the spatial analysis of immune cell subclusters highlighted a special niche composed of T cells and PIM, Mono which co-localized with HFSC and PF (large wound margin and large wound center).

Cellular communication landscape between immune cell and HF-related cutaneous cell

Since most signaling pathways are activated through ligands diffusing from sender cells or direct physical contact with nearby receiver cells, cell signaling is spatially constrained [41] (Fig. 5A). Based on the integration profiling of scRNA-seq and ST, we observed the co-localization of T cell, PIM, and Mono with the PF and HFSC in large wound center and wound margin (Fig. 4D~4F), which laid the foundation the potential cellular communication among them.

Next, to address potential interactions between those spatially colocalized cell populations, Cell Chat[42] was applied to predict the cell-cell communication patterns at the level of ligand/receptor expression (Fig. 5B). The expression of signal molecules was next verified by visualizing the major ligands and receptors in ST sections. By comparing

the interaction strength (information flow), we could identify signaling pathways decrease (turn-off) or increase (turn-on) in different biologic conditions. As shown in Fig. S6, the bar graph showed significant signaling pathways ranked based on differences in the overall information flow. The top signaling pathways colored red were enriched in Ctrl_LW. Next, we selected those up-regulated pathways and compared the overall signaling strength of ligand-receptors that exhibit different signaling patterns (Fig. 5C). Consistent with the result of bulk-seq, adaptive immune system related pathways including MHC-I, MHC-II and CD80 was exclusively enriched in large wound. The major signaling among immune cell and cutaneous cell in large wound was mediated by PF (origin of de novo HF). Immune cells near PF, HFP and HFSC were enriched for interacting receptor or ligand gene partners such as Il6/Il6st, Inhba/Acvr1b. As shown in Fig. 5 D, NKT2, γδ T, Th17 as well as PIM in large wound increased the expression of Il6 (major ligand in IL6 signaling pathway). Correspondingly, the PF1 and PF2 and HFSC in large wound also expressed the Il6st (major receptor in IL6 signaling pathway). What’s more, PIM, and Mono in large wound significantly up regulated the expression of Inhba (major ligand in ACTIVIN signaling pathway). Similarly, PF1 and PF2 and HFP in large wound also exclusively expressed the Acvr1b (major receptor in ACTIVIN signaling pathway). Spatial plots showed the preferentially aggregation of Il6 and

Inhba in large wound margin and center (co-localized with HFSC, PF as well as PIM, Mono, T cells). The essential role of activin[43,44] and Il6[12] pathway in HF regeneration has been reported. Our result illustrated that immune cell especially PIM, Mono and T cells may modulate the states of PF, HFP and HFSC through signaling pathways such as IL-6 and activin.

Together, these results uncovered the spatial heterogeneity of immune cell exclusively residing in the center and margin of large wound and highlighted potential intercellular signaling pathways controlling the states of HF precursor cells. The communication between immune and cutaneous cells was sophisticated, and these results might serve as a resource for further investigation of immune dynamics in scar-less skin regeneration.

More abundant neogenic HFs occurred in scaffold-implanted wounds with the further activation of adaptive immune system

Synthetic graft transplantation is one of the efficient treatments for severe large area wound of skin especially when patient's donor site is not qualified[3]. With the further understanding of tissue engineering, it is suggested that synthetic materials imitating the native structure of native ECM structure can integrate and play potentially pro-regeneration role to wound healing[15,45]. Our previous report has illustrated the pro-regenerative immuno-regulatory effect of aligned electrospinning scaffold

with approximate 300nm diameter fibers in small wound (diameter=0.6cm) healing[18,19]. We wonder if the polymer ECM scaffold exerts the similar pro-regenerative effect in large wound which required better flexibility, biocompatibility, degradability. Besides, the scaffold-mediated immune microenvironment in large wound healing still needs further understood.

We next repeated large full-thickness wound-healing experiments in C57BL/6 mice with/without implanted electrospinning membrane to investigate if the further regenerative phenomenon observed in ECM biosynthetic scaffold treated wounds. Workflow for evaluating large wound healing in C57BL/6 mice was summarized in Fig. 6A. We placed synthetic ECM scaffolds below the full-thickness excisional wound (diameter,1.5 cm; Fig. 6B) in ECM_LW group, while the Ctrl_LW group received no materials.

Wound coverage was faster in the ECM_LW group on POD7 (Fig. 6, C and E). The ECM_LW also had the smaller gap width on POD7 and POD14 (Fig. 6. D and F). IF staining for cytokeratin 5 (Krt5) and cytokeratin 10 (Krt10) confirmed that ECM_LW group had the larger area of neo-epithelium (Fig. 6K). Consistent with our previous report[19], the ECM membrane implanted in large wound did not trigger an obvious fibrous capsule (Fig. S7). In addition, the scaffold owned a rapid degradation rate in vivo. We could observe the degrading fragments on

POD 14 and degrading particles on POD21, and there were not any visible remaining on POD28 (Fig. S7) The outline of HF morphology could be recognized in ECM_LW group (Fig. 6D): with the first appearance in hair germ stage on POD7, they gradually grew into bulbous-peg structure overlaid the degrading scaffold fragments on POD14. On POD28, we found that ECM_LW group recapitulated normal skin architecture with equivalent number of mature appendages and “basket-wave” ECM collagen deposition (Fig. 6D). Intriguingly, most de novo hair follicle in wound site was zigzag without pigmentation (Fig. 6B). In summary, in mouse large full-thickness wound models, the aligned electrospinning membranes led to faster wound healing and enhanced regeneration of HF. The excellent biocompatibility and degradability of membrane also avoid the risk of immune rejection and secondary surgery in further clinical applications.

Subsequently, bulk-seq was performed for ECM_LW and Ctrl_LW samples harvested on POD7. Compared to the Ctrl_LW, the ECM_LW group showed increased enrichment of genes involved in the hair follicle development as well as T cell differentiation (Fig. 6H). KEGG analysis revealed elevated gene expression in leukocyte transendothelial migration pathway for the ECM_LW group (Fig. 6H). Meanwhile, the volcano plot showed up-regulated genes in ECM_LW group which related to the further activation of adaptive immune system (Fig. 6I). IF and IHC

staining for Cd3 confirmed the increased T cell infiltration with implanted scaffold on POD 7 (Fig. 6J).

Sc-RNA revealed higher proportion of dermal condensate and HFP in scaffold-implanted large wound

To explore how ECM scaffold regulated the microenvironment in large wound, we isolated cells from the ECM_LW and Ctrl_LW samples and applied them to the 10x scRNA-seq platform (Fig. S8A). After cell filtering, 31,740 single-cell transcriptomes were included in the final dataset (20,312 for the ECM_LW group and 11,428 for the Ctrl_LW group). Unsupervised clustering using Seurat categorized the cells into 10 main classes of cells. The composition of each cell cluster was listed so that the proportion of cells from two groups could be identified across all cell clusters (Fig. S8B). Marker genes for each cell cluster were shown in the heatmap in Fig. S8C. Genes related to T cells (Il7r, Areg and Tubb5) were substantially higher expressed by the ECM_LW (Fig. S8D).

Firstly, As shown in Fig. 7A, we defined most fibroblast subclusters based on defined markers in Fig. 2B. Remarkably, we identified the $Smad3^{+}Lef1^{+}Krt17^{+}$ dermal condensate (Dc) cell[46] specially in this dataset. Derived from PF, The Dc was believed to be the origin of DP reside at the base of the adult HF [46,47].Since approximate 90% of Dc were from ECM_LW group, as well as significantly higher proportion of $PF1^{2}$ and $PF2^{2}$ from ECM_LW (Fig. 7B), which might provide enough

mesenchymal component for the subsequent HF formation in ECM_implanted group.

In embryologic HF morphology, Dc is believed to be the signaling niches for epithelial HFP to form epithelial placode (Pc)[46], and thus promote HF growth. In our subcluster analysis of keratinocyte based on known marker in Fig. 2F, we also find the higher proportion of HFP^2 and $HFSC^2$ in ECM_LW group (Fig.7), which might serve enough epithelial resources for nascent HF growth. What's more, the higher proportion of interfollicular epidermal basal $cell^2$ ($IFEB^2$) and interfollicular epidermal differentiated $cell^2$ ($IFED^2$) were observed in the ECM_LW group, supporting more neo-epithelium proliferation in the presence of scaffolds. Increased epithelialization in large wound healing with implanted scaffold was confirmed in IF staining of Krt5 and Krt10 (Fig.6K).

Analysis of immune cells heterogeneity induced by implanted scaffold in large wound healing

As shown in Fig. S8B, the implantation of ECM scaffold seems does not induce a strong inflammatory response but has an impact on adaptive immune cell polarization, potentially inducing regenerative phenotypes.

Firstly, activated by platelets, neutrophils are the first responding immune cells acting as the critical mediators of innate immune system. They are necessary for the degradation of biomaterials as well as recruitment and differentiation of monocytes[48]. Four neutrophil subsets

including Il1b^{+}Retnlg^{+} peripheral blood neutrophil (PBN^{2}), Il1a^{+}Tnf^{+} neutrophil1 (Neu1), Lrg1^{+}Il1r2^{+} neutrophil2 (Neu2), Ccl9^{+}Rgs1^{+} neutrophil3 (Neu3) were identified in our dataset (Fig.S8, A~B). KEGG analysis showed the PBN^{2} was enriched in mitophagy, which was essential for neutrophil differentiation[49]. Neu1 and Neu2 were respectively related to phagosome and Fc-gamma R mediated phagocytosis. While Neu3 showed gene enrichment in leukocyte migration and Th17 cell differentiation. Neu3 was the only subsets owned a higher proportion in ECM_LW group (Fig.S8 C).

Dendritic cell (DC) was classified into two subclusters including Krt5^{+}Krt14^{+} langerhans cell (LC) and Cd86^{+} monocyte derived dendritic cell (MDC) (Fig.S8, D~E). KEGG analysis showed that LC and MDC respectively related to phagosome and antigen presentation (Fig.S8 F). There was no obvious difference in the proportion of DC subsets between the two groups.

Macrophages were of vital importance in orchestrating biomaterial related FBR and tissue regeneration[50]. Three subsets of macrophages including (Ccl8^{+}Folr2^{+}C1qa^{+}Mrc1^{+}) AIM^{2}, (Mmp12^{+}Arg1^{+}Inhba^{+}Nos2^{+}) PIM^{2} and (Ly6c2^{+}Plac8^{+}Cytip^{+}H2-Eb1^{+}) Mono^{2} were determined. The Ctrl_LW group contributed to a larger proportion of all three subsets, suggesting that the scaffold might play a role in the reduction of macrophage infiltration at the proliferative stage (Fig.8 A~C).

T cells were the only immune cell which owned a higher proportion in ECM_LW group (Fig.S8 B). Subclustering of T cells resulted in seven subsets (Fig.8 D). In addition to Cd8b1^{+} cytotoxic T cell^{2} (CTL^{2}), (Tyrobp^{+}Nkg7^{+}Xcl^{+}) nature killer cell^{2} (NKT^{2}), (Il17a+Il17f^{+}) T helper17^{2} (Th17^{2}), Foxp3^{+} T regulatory cell^{2} (Treg^{2}), and (Trdv4^{+}Cd7^{+}Ctsw^{+}) γδT cell^{2} (Tγδ^{2}) which had been defined in Fig.3 G, two new immune cell subclusters including (Bcl11a^{+}Id3^{+}Notch1^{+}) innate lymphoid cell (ILC) and (Gata3^{+}Il5^{+}) T helper2 (Th2) cell were identified in our dataset based on published research[51,52]. Derived from common lymphoid progenitors, ILCs mirror αβ T cell subtypes functionality responding to local signals but lack antigen-specific receptors. In skin, tissue resident ILCs play key roles in barrier integrity, inflammatory response initiation, and immunological response modulation in wound repairing[52-55]. Correlation analysis showed that ILC and Th2 were respectively highly correlated with CTL^{2} and Th17^{2} (Fig. 8E). Remarkablely, skin-resident ILC in our dataset possessed a tissue specific transcriptional profile that co-expression genes related to T cell functionality (Cd3d^{+}Klf4^{+}Fst^{+}Itga6^{+}) and HF morphology (Wnt4^{+}Sox9^{+}Fgfr2^{+}). Gene enrichment analysis showed the ILC was related to bacterial invasion of epithelial, leukocyte transendothelial migration as well as hair follicle development (Fig.8, G~H). It was suggested that ILCs might initiate HF neogenesis by balancing reparative

and pro-inflammatory function[56]. Collectively, our dataset suggested that ECM-scaffold exerted the immune-regulatory effect on the further activation of adaptive systems in large wound healing, which might play role in HF development.

Integration of ST and sc RNA-seq illustrated the cell heterogeneity in ECM_LW group

Subsequently, to explore the spatial characteristic of cell heterogeneity in scaffold-implanted wound, we also applied the ST to analyze spatial gene expression profiles of ECM_LW group and Ctrl_LW group on POD7 (Fig. 9A). Although generally the HF formation procedure would not start until several days after wound closure in large wound without implantation (POD14~21) [5]. In ST profiling of ECM_LW group on POD7, we could identify the initial structure of HF composed of Krt28^{+}HFP in neo-epidermis and Twis2^{+} Dc aggregation beneath in dermis (Fig. 9C). In the first wave of embryonic HF formation, the Dc would secrete signals to induce the proliferation of HFP into Pc. Undergoing Pc/Dc stage, hair germ stage, hair peg stage, hair bulbous peg stage, and hair follicle stage, eventually the Dc would be engulfed by the HF matrix developed by Pc and transition into the mature DP[57]. In summary, our ST profiling highlighted the early HF formation signature in ECM_LW group at the spatial gene expression level (Fig.9 D).

Next, the top50 marker genes of each fibroblast subclusters from

scRNA-seq (defined in Fig.7 A-D) were used to score each ST spots of ECM_LW and Ctrl_LW. Spatial plot showed that the distribution of upper lineage PF (origin of Dc) was enlarged in ECM_LW group. In contrast, lower lineage fibroblasts including RF and LF (related to collagen deposition) were significantly reduced with implanted membrane (Fig.9 F). The spatial heterogeneity of fibroblast subclusters between ECM_LW and Ctrl_LW might account for the different healing outcome after that.

To explore the scaffold-induced immune microenvironment, we next integrated the marker genes of immune cells with ST profiling. Spatial plot of each cluster in ST sections were shown in Fig. 9F. We noticed the robust accumulation of neutrophils within and around the membrane which outlined the shape of implanted scaffold. The adhesion of neutrophils might lead to an enhanced degradation of scaffold and recruit the MAC later[48]. The obvious aggregation of MAC surrounding the membrane could be observed, but not infiltrated into the scaffold. As shown in Fig. S11A, IHC staining for Cd68 confirmed the recruitment of the macrophages without the fusion of foreign body giant cell (FBGC). The Masson's trichrome staining for ECM_LW group on POD 7 did not show excessive fibrous capsule around the scaffold as well (Fig. S8), suggesting the good biocompatibility of aligned membrane in large wound healing.

Outside the macrophage, we could identify the enlarged distribution of dendritic cell and T cell in ECM_LW group. Notably, we observed the accumulation of tissue resident ILC in epithelium as well as granulation tissue particularly in ECM_LW group. ILCs in close proximity to keratinocyte might potentiated the cellular communication with HFSC or HFP cells, and thus help HF formation. IHC staining for Cd3 identified the skin-resident T cells in neo-epithelium and confirmed the recruitment of the migrating T cell surrounding or beneath the implanted scaffold in ECM_LW group. $Cd3^+$ T cell have also been detected in Ctrl_LW group, but they were present in low proportions and limited in granulation tissue center (Fig. S11B). It was noteworthy that other T cell subclusters, PIM (related to pro-inflammatory response) and Mono (related to antigen presentation) were significantly enlarged in ECM_LW group, overlapping with the distribution of PF (Fig. 10F).

Prediction of critical signaling patterns between spatially colocalized cell populations of ECM_LW and Ctrl_LW

The detailed impact of scaffold-induced immune microenvironment on the large wound healing and underlying signaling controlling HF formation remained unknown. Based on the multimodal profiling, we still observed the overlapping distribution of T cell, PIM, and Mono with the HF precursor cells in ECM_LW group (Fig. 9E and Fig. 10F), which implied the potential cellular communication among them.

Next, we applied Cell Chat to predict the cell-cell communication patterns between EMC_LW and Ctrl_LW (Fig. 10 A and B). The heatmap showed the overall signaling strength of ligand-receptors in Ctrl_LW and ECM_LW group (Fig. 10C). Consistent with the result of bulk-seq, adaptive immune system related pathways including MHC-II was activated in ECM_LW. In addition to IL6, the key signaling in embryonic HF development such as FGF[46], Notch[58], KIT [42] were up-regulated in ECM_LW group. Remarkablely, T cell subclusters (especially ILC) and HF precursor cell were enriched for interacting receptor /ligand gene partners including Areg-(Egfr+Erbb2), Epgn- Egfr. As shown in Fig. 10 D, ILC, Treg^2, γδ T^2, Th2^2, Th17^2 in large wound increased the expression of Areg (major ligand in Egf signaling pathway), while the ILC particularly expressed the Epgn (major ligand in Epgn signaling pathway). Correspondingly, the Dc, HFSC^2, HFP^2, PF1^2 and PF2^2 also expressed the Egfr and Erbb2 (major receptor in Egf and Epgn) signaling pathway). Spatial plots supported the aggregation of Epgn and Egfr (co-localized with ILC^2). Epgn (Epithelial Mitogen) was a member of the epidermal growth factor (Egf) family. The critical functions of Egf pathway in embryogenic skin morphologies has been predicted[42], and the expression of epidermal growth factor receptor (Egfr) was believed to be essential for Treg cells to facilitate cutaneous wound healing[59]. Based on our multimodal analysis, the T cells (especially ILC) might modulate

the HF precursor cell growth through EGF and EGPN pathways, and thus facilitate the HF formation.

In addition, as shown in Fig. 10E we observed that the immune cells (macrophage and T cell subclusters) and HF precursor cell were enriched for interacting receptor or ligand gene partners including Mdk-(Sdc1 or Itgb1), Ptn-(Itgb1or Sdc1). The role of pleiotrophin (PTN) and midkine (MK) pathways in mice epidermal stratification event occurred between E13.5 and E14.5 was stressed[42].Based on our prediction, HF precursor cells could reversely mediate the activation of immune cell through regional cellular communications such as Mk and Ptn pathways as well.

In summary, these results uncovered the spatial heterogeneity of immune microenvironment induced by implanted scaffold in large wound healing. We identified the enlargement of “pro-regenerative” immune niche co-localized with the HF precursor cells and predicted possible cell-cell communication among them. These regional signaling pathways might be the potential mechanism to for immune cells to control the HF fate specification, and thus prompt the nascent HF regeneration in scaffold-implanted group.

Aligned scaffold facilitated the de novo HF regeneration despite of wound size

To detect if there still any difference in wound healing between small or large wound treated with biomaterial, we next repeated small

(diameter=0.6cm) and large (diameter=1.5cm) full-thickness wound implanted with electrospinning membrane (Fig.S12 A and B).

Consistent with ECM_LW group, the aligned membrane implanted in small wound did not trigger an obvious FBR fibrous capsule either (Fig. S12C). There was no significant difference in thickness of fibrous capsule around scaffold between small and large wound (Fig. S12D). The scaffold still owned a rapid degradation rate in small wound. We could identify the degrading fragment on POD14, and there was not any visible remaining on POD28 (Fig. S12C). In addition, histological sections of the ECM_SW tissue also revealed clear signs of enhanced WIHN (Fig. S12C): On POD14, neo-epithelium of small wounds displayed bulbs and under there were several epidermal cysts, while the dermis was thicker wrapping the degrading scaffold fragments. Subsequently, we observed mature HFs featured SG on POD28 (Fig. S12E). Similarly, de novo hair follicle in ECM_SW group was zigzag without pigmentation (Fig. S12E). The difference of average HF numbers between two groups was not statistically significant as well.

Based on bulk-seq profiling, heatmaps showed insignificant changes of gene expression related to HF regeneration, adaptive immune response, or innate immune response (Fig. S12G). IHC staining for Cd3 and Cd68 confirmed the resembling infiltration level of T cell and macrophage surrounding the scaffold or in granulation tissue (Fig. S12 H and I).

We further explored the differences in immune cell composition using scRNA-seq (Fig. S13A). Unsupervised clustering categorized the cells into 11 main clusters, and marker gene for each cluster was shown in Fig. S13B. Subclustering of macrophages resulted in three subsets, which were PIM^3, AIM^3 and $Mono^3$ (Fig. S13C). Although the Ctrl_SW samples had the lower number of $Mono^3$ ($Ly6c2^+Cytip^+H2\text{-}Eb1^+$) but recruited more AIM^3 ($Folr2^+C1qa^+Mrc1^+$) and PIM^3 ($Inhba^+Il1a^+Clec4e^+$) (Fig. 8D). The total proportion of macrophage was equilibrium between two groups (Fig. S13A), and the integrated analysis of ST profiling showed the similar distributions of three subsets around the scaffold (Fig. S13G). Subclustering of T cells resulted in six subclusters. According to the marker genes, the T cell subsets were named $\gamma\delta T^3$ ($Cd7^+Ctsw^+$), $Treg^3$ ($Foxp3^+$), $Th17^3$ ($Il17a^+$), ILC^3 ($Id3^+Notch1^+Fst^+$), NKT^3 ($Gzma^+$ $Xcl1^+$), and CTL^3 ($Cd8b1^+$) (Fig. 13 D and E). The Ctrl_SW group had the lower proportion of NKT^3 and ILC^3, but recruited more $\gamma\delta T^3$, $Treg^3$, $Th17^3$ and CTL^3. Despite the slight difference in T cell subclusters composition, multimodal analysis confirmed the substantial distribution of all T cell subsets surrounding the scaffold in both groups (Fig. S13H).

In summary, based on our evaluation, the aligned electrospinning membrane with good biocompatibility showed similar “pro-regenerative” effect on would healing despite of wound size. Besides, the resembling

immune-regulatory effect on adaptive immune system indicating the significant role of local immune environment in HF regeneration.

Discussion

Problems including delayed would closure, susceptibility to infection, and inability of regenerating appendages have become the main impediment for skin wound healing[1]. Requirements for appropriate biocompatibility, degradability, and ability to accelerate epithelialization as well as promote nascent HF formation bring significant challenges to biomaterial design, particularly for large-scale full-thickness wound. WIHN is a rare model of mammalian organ regeneration in adult mice wherein large full-thickness wound (>1cm^2) induce few nascent HF regeneration limited in wound center[5]. The initiation of HF morpho genesis begins when the HFP[33] and HFSC[10] migrating with neo-epithelium and induced the aggregation of Dc (derived from PF) under them[60]. The pro-regenerative influence of the immune system in coordinating the early stage of wound repairing has been stressed[61]. However, the cellular interplay between specific immune subclusters and HF precursor cells remains unclear.

Here, we firstly compared the transcriptomics profiles between total “scarring” (small wound, diameter = 0.6cm) and “half-regenerative” WIHN (large wound, diameter = 1.5cm) model. From our multimodal analysis of small (Ctrl_SW) and large wound (Ctrl_LW) samples, we

observed the higher proportion of adaptive immune cell from Ctrl_LW group (Fig. 4F), which resided in large wound center and margin co-localizing with HF precursor cells (Fig. 4 C and D). The active regional cell-cell communications among them indicated the “pro-regenerative” role of local immune niche[62] in promoting HF neogenesis and served as a promising therapeutic target for the application of immune-regulatory materials in skin wound regeneration (Fig. 5 D and E).

Next, we employed the biosynthetic PLGA/FC electrospinning membrane for large area skin defect along with the investigation of its role in wound healing and immune microenvironment modulation. The scaffold showed the impact on accelerating wound closure and promoting the nascent HF formation (Fig. 6 E and G). It was shown that the biodegradable scaffold did not induce a strong FBR (Fig. S8) but owned a regulatory impact on adaptive immune system. We identified that the substantial T cell infiltration in response to scaffold implantation was driven toward regenerative subpopulations, overlapping with the abundant PF (origin of Dc) (Fig. 9E and Fig. 10F). The local intercellular communications among the enlarged “pro-regenerative” immune niche with HF precursor cells supported the essential role of adaptive system in HF regeneration (Fig. 10 D and E).

Lastly, we confirmed the pro-regenerative effect of scaffold in both small and large wound repairing (Fig. S12F). The scaffold showed the

resembling effect on the recruitment of T cells (Fig. S12H and Fig. S13J). Meanwhile, the mild FBR around the scaffold decreased the risk of immune rejection, and the appropriate degrading rate could also avoid the extra expense of secondary surgery (Fig. S12 C and D). In conclusion, this easy-fabricating biodegradable scaffold offered an available manner to regenerate skin in severe damage through modulating the adaptive immune system.

There still were several questions to be addressed further. Firstly, the primary stimulator driving the preferential aggregation of immune cells was unknown and it may be either molecular[17] or mechanical[63]. Secondly, specific cellular signaling pathways between immune cells and cutaneous cells need further verified. Lastly, usually unpigmented hairs were regenerated when the wound was created during the telogen/catagen stage of hair cycle[5,64]. It deserved subsequent exploration about the activity of melanocytes in WIHN model.

Figure legends

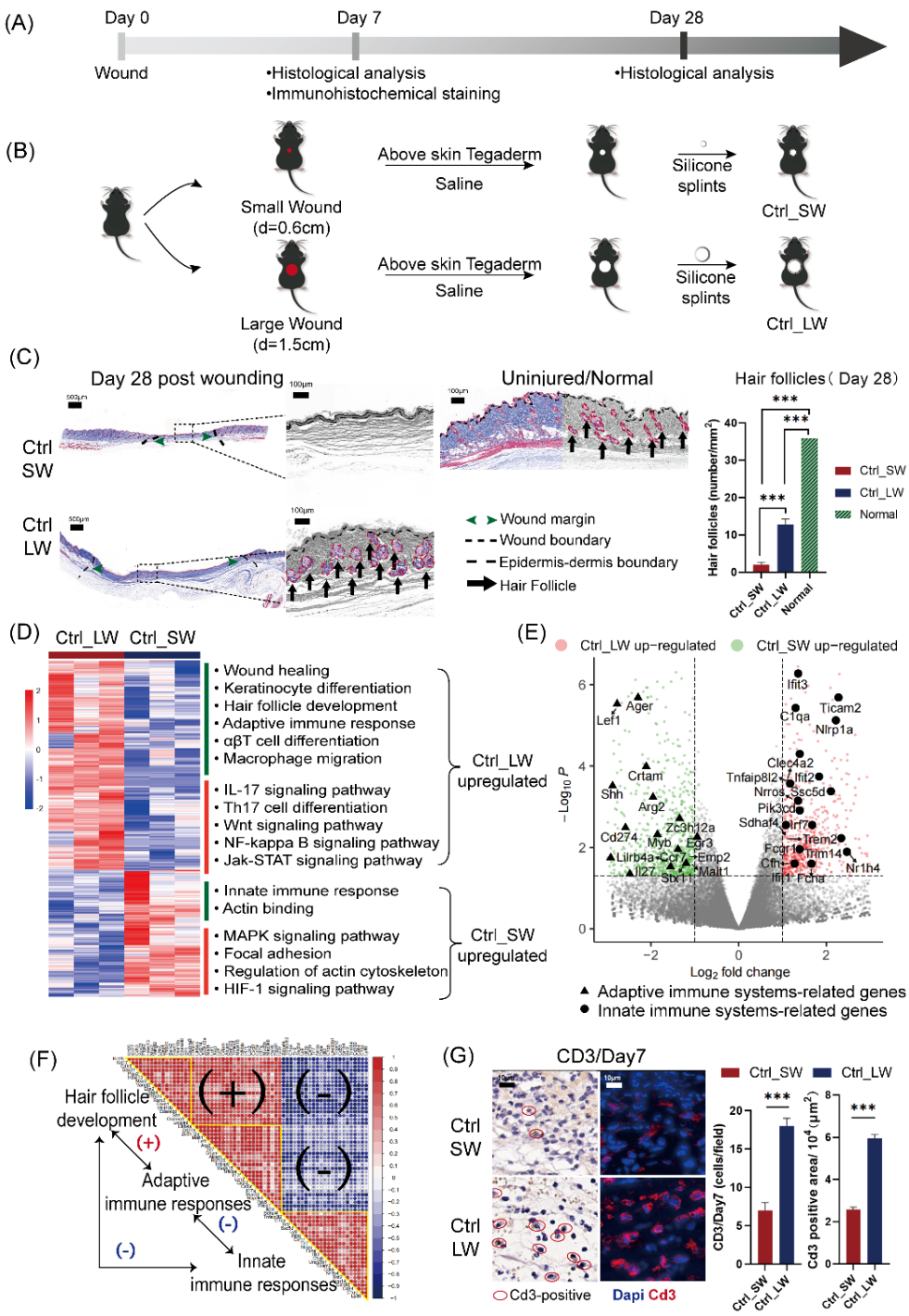

Fig.1. Evaluation of the healing of small and large full-thickness wound. (A) Workflow for evaluating mice skin wound healing. (B)

Surgical process for the mice full-thickness excisional splinted wound. (C) Haematoxylin and eosin (H&E) staining of normal skin or healed small (Ctrl_SW) and large (Ctrl_LW) full-thickness skin wound on POD 28, and histologic quantification of de novo hair follicles. (D) Heatmap showing hierarchical clustering of differentially expressed genes (p value<0.05 & |log2FC|> 1) and gene set enrichment analysis showing the up-regulated GO (green) and KEGG (red) pathways between two groups. (E) Volcano plot showing interested differentially expressed genes between two groups (bulk seq). (F) Pearson correlation analysis shows positive correlation between the expression of hair follicle development related genes, adaptive immune responses related genes and innate immune responses related genes (positive, red; negative, blue). (G) IF staining and IHC staining of Cd3 in wound center and corresponding quantification of $CD3^+$ cellular infiltration.

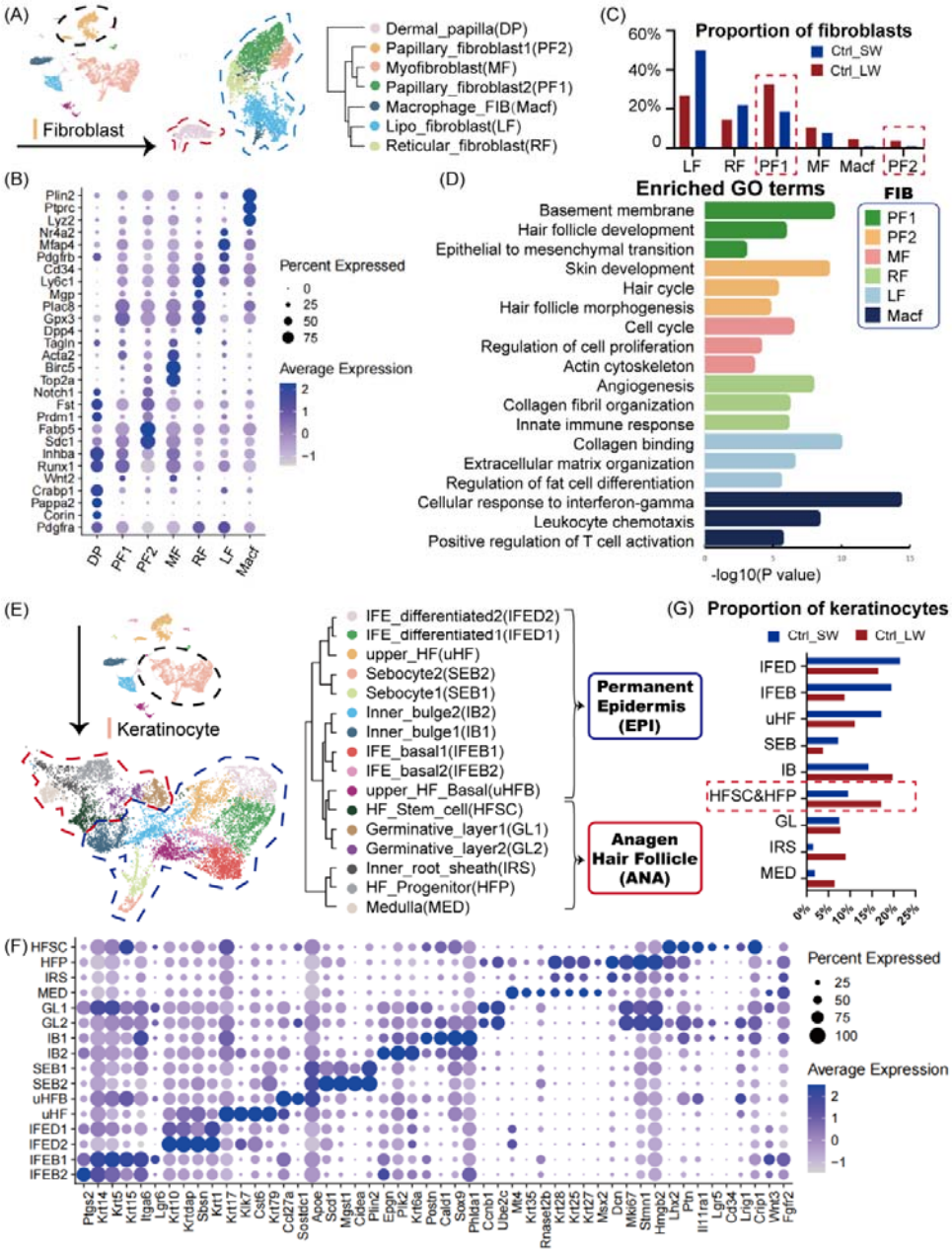

Fig.2. Further analysis of fibroblasts and keratinocytes between Ctrl_SW and Ctrl_LW. (A) Subclustering of fibroblasts showing 7 subsets and hierarchical clustering of average gene expression using pearson correlation analysis. (B) Marker genes for each fibroblasts subset. (C) Proportion of each subset in two groups. (D) GO enrichment analysis

of wound fibroblast subtypes. (E) Subclustering of keratinocytes showing 16 subsets and hierarchical clustering of average gene expression using pearson correlation analysis. (F) Marker genes for each keratinocytes subset. (G) Proportion of each keratinocytes subset in two groups.

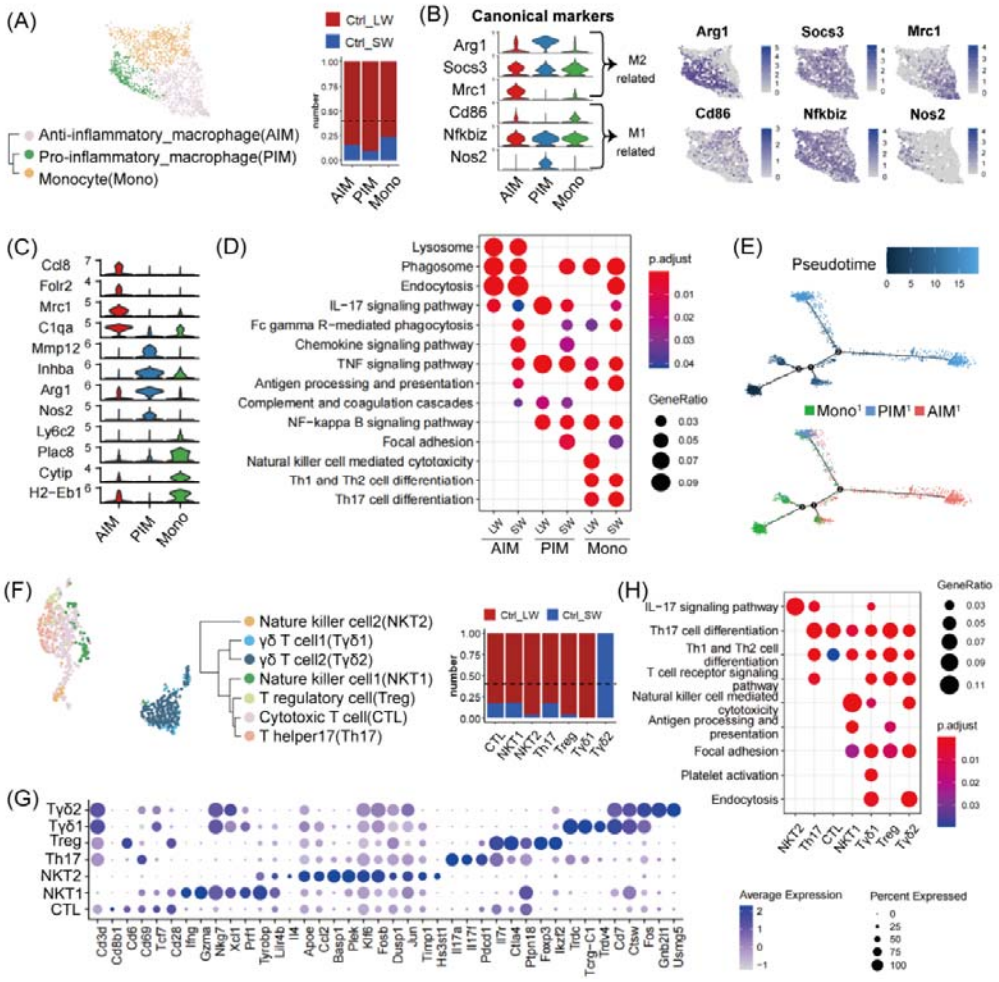

Fig.3. Analysis of MAC and T cells between Ctrl_SW and Ctrl_LW.

(A) Subclustering of MAC showing three subsets and hierarchical clustering of average gene expression (pearson correlation analysis); The composition for each subset. (B) Expression of canonical M1 and M2 markers was inappropriate to identify the subtypes. (C) Marker genes for each MAC subset and (D) gene set enrichment analysis in KEGG pathway. (E) Pseudo-temporal ordering and the distribution of MAC subsets. (F) Subclustering of T cells showing seven subsets and hierarchical clustering of average gene expression (pearson correlation

analysis); The composition for each subset. (G) Marker genes for T cell subsets and (H) gene set enrichment analysis in KEGG pathway.

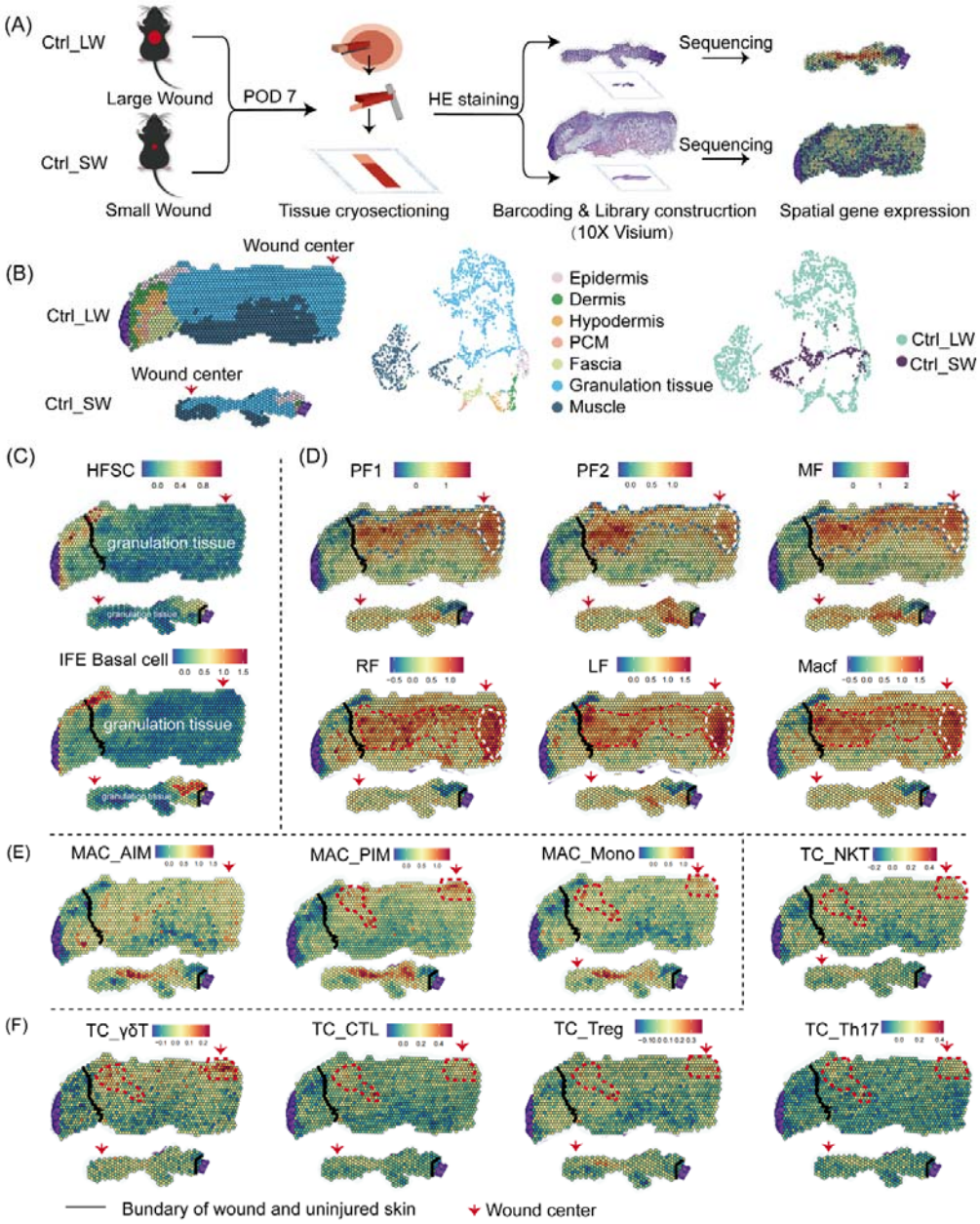

Fig. 4. Spatial transcriptomics applied to Ctrl_SW and Ctrl_LW. (A) Schematic for generating spatial transcriptomics data from splinted excisional wounds. Fresh wound tissue was harvested, flash frozen, embedded, and H&E staining. Each spot contained mRNA expression

profiles of 1~10 cells. (B) Spatial plots and UMAP plot showing that the seven regions could be distinguished by their transcriptional programs. Spatial feature plots showed defined keratinocyte (C), fibroblast (D), MAC (E) and T cell (F) subclusters distribution in tissue sections using Addmodulescore. Based on histological image, we could identify the wound center (red arrow) and separate the neo-epidermis migrating above the granulation tissue from unwound epidermis above the normal dermis away from the wound (black solid line).

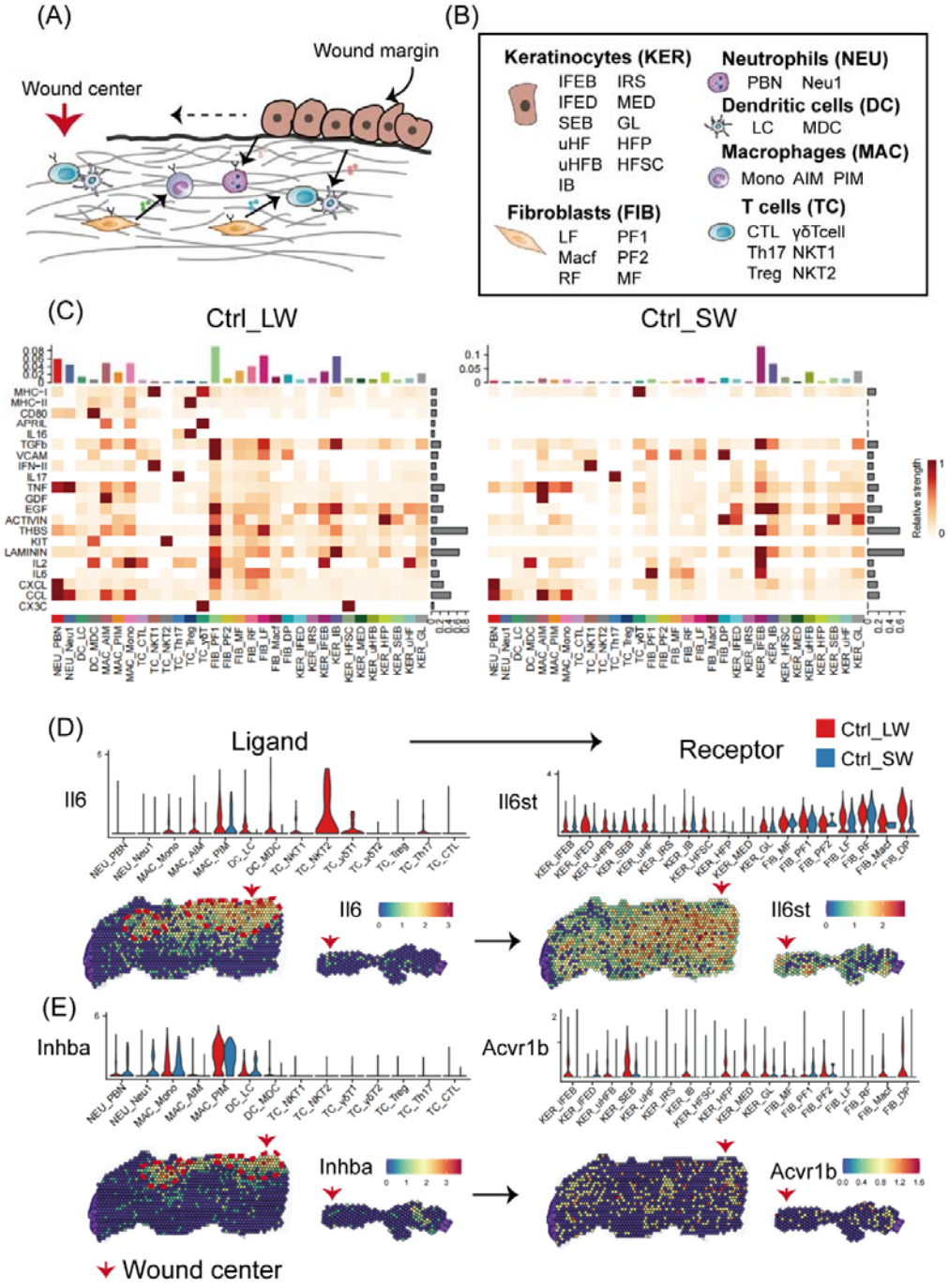

Fig. 5. Cellular communication landscape between immune cells and cutaneous cells in Ctrl_SW and Ctrl_LW. (A) Schematic of combined ligand-receptor analysis between keratinocytes, fibroblasts, and immune

cells. (B) Defined subclusters in our scRNA-seq dataset. (C) Comparison of cell-cell communication patterns between Ctrl_SW and Ctrl_LW using CellChat. (D) Violin plot (sc-RNA) and spatial feature plots (ST) showed select ligands expressed by immune cell subpopulations and cognate receptor expression by keratinocytes and fibroblasts subtypes.

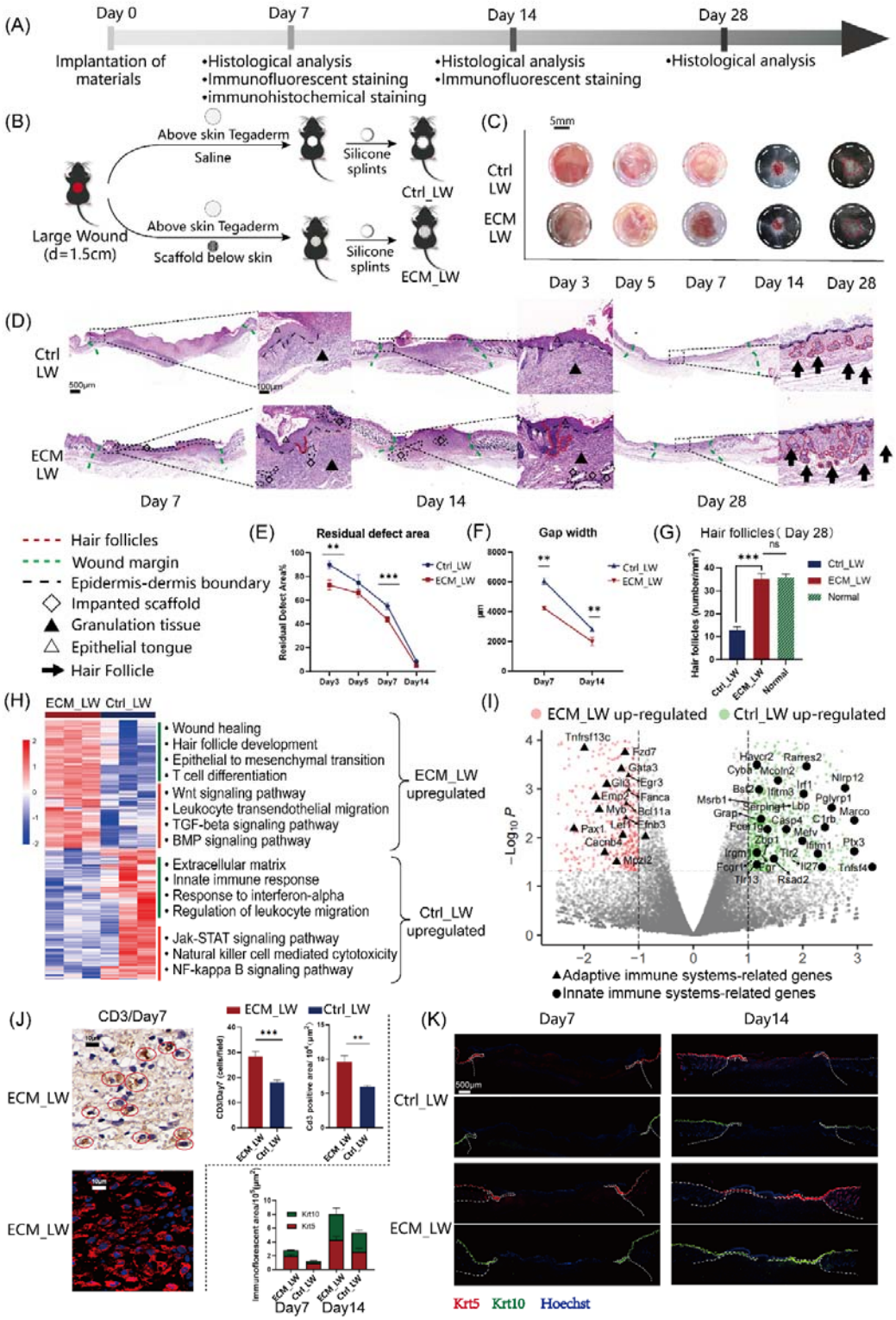
(A)
Day 0
Day 7
Day 14
Day 28
Implantation of materials
•Histological analysis
•Immunofluorescent staining
•immunohistochemical staining
•Histological analysis
•Immunofluorescent staining
•Histological analysis
(B)
Above skin Tegaderm
Saline
Silicone splints
Ctrl_LW
Large Wound (d=1.5cm)
Above skin Tegaderm
Scaffold below skin
Silicone splints
ECM_LW
(C)
5mm
Ctrl LW
ECM LW
Day 3
Day 5
Day 7
Day 14
Day 28
(D)
Ctrl LW
ECM LW
Day 7
Day 14
Day 28
Hair follicles
Wound margin
Epidermis-dermis boundary
Impanted scaffold
Granulation tissue
Epithelial tongue
Hair Follicle
(E)
Residual defect area
Residual Defect Area%
Ctrl_LW
ECM_LW
Day3
Day5
Day7
Day14
(F)
Gap width
Ctrl_LW
ECM_LW
Day7
Day14
(G)
Hair follicles (Day 28)
Hair follicles (number/mm²)
Ctrl_LW
ECM_LW
Normal
(H)
ECM_LW Ctrl_LW
• Wound healing
• Hair follicle development
• Epithelial to mesenchymal transition
• T cell differentiation
• Wnt signaling pathway
• Leukocyte transendothelial migration
• TGF-beta signaling pathway
• BMP signaling pathway
ECM_LW upregulated
• Extracellular matrix
• Innate immune response
• Response to interferon-alpha
• Regulation of leukocyte migration
• Jak-STAT signaling pathway
• Natural killer cell mediated cytotoxicity
• NF-kappa B signaling pathway
Ctrl_LW upregulated
(I)
ECM_LW up-regulated
Ctrl_LW up-regulated
−Log10 P
▲Adaptive immune systems-related genes
●Innate immune systems-related genes
(J)
CD3/Day7
ECM_LW
ECM_LW
Ctrl_LW
CD3/Day7 (cells/field)
Cd3 positive area
Krt10
Krt5
Immunofluorescent area
Day7
Day14
(K)
Day7
Day14
Ctrl_LW
ECM_LW
Krt5
Krt10
Hoechst

Fig. 6. Evaluation of the healing of large full-thickness wounds with implanted ECM scaffolds. (A) Workflow for evaluating mouse large-scale wound healing. (B) Surgical processes for mouse skin excisional wound model. (C and E) Residual wound area at 3, 5, 7, 14 and 28 days, and corresponding analysis. (D) H&E sections of two groups. (F) Semiquantitative evaluation of gap width. (G) Histologic quantification of de novo HFs on POD28. (H) Heatmap showing hierarchical clustering of differentially expressed genes (p value<0.05 & |log2FC|> 1) and gene set enrichment analysis showing the up-regulated GO (green) and KEGG (red) pathways between two groups. (I) Volcano plot showing interested differentially expressed genes in two groups (bulk seq). (J) IF staining and IHC staining of Cd3 in wound center and corresponding quantification of $CD3^+$ cellular infiltration. (K) IF staining using Krt5 (red) and Krt10 (green) and semiquantitative evaluation of the fluorescent area.

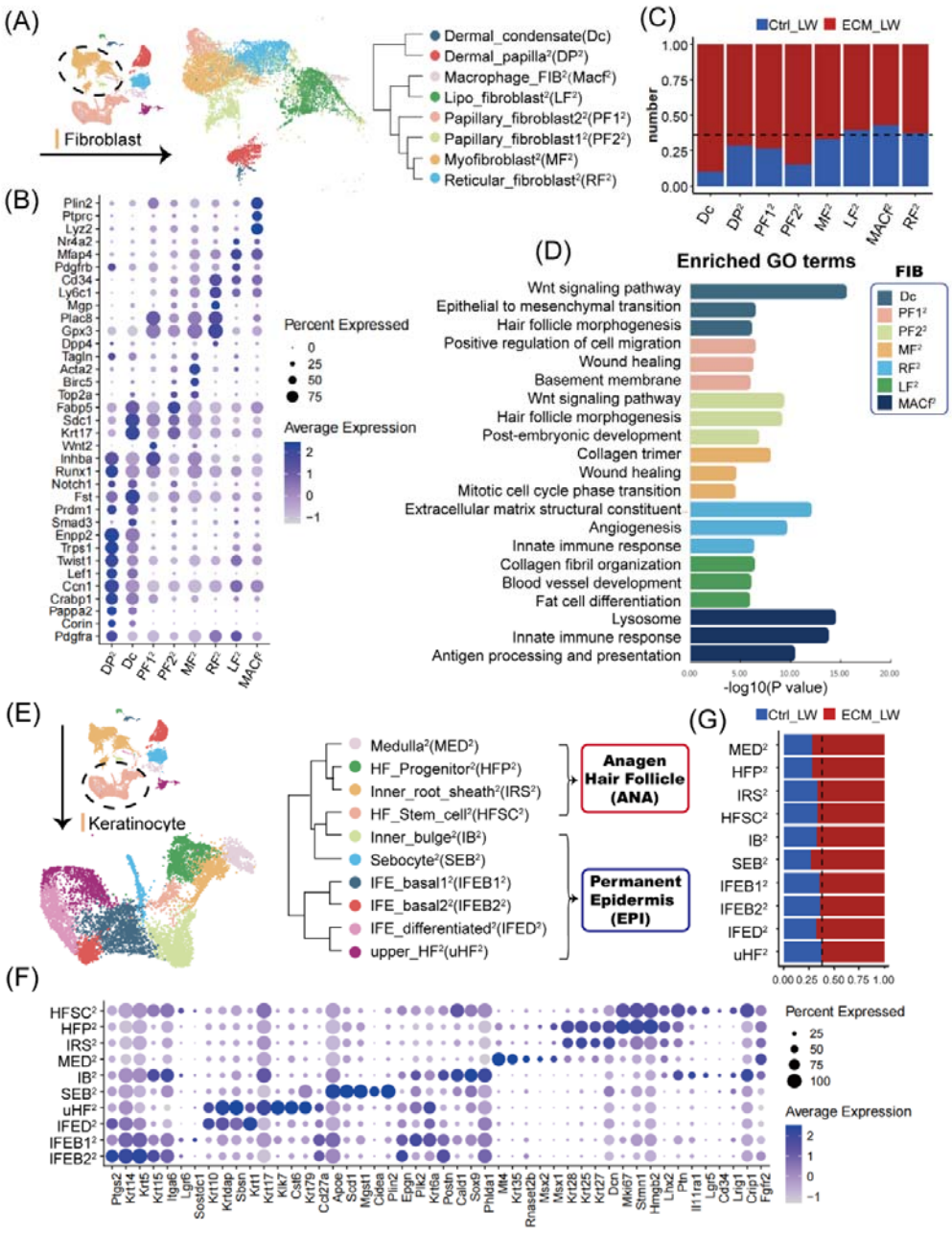

Fig. 7. Further analysis of fibroblasts and keratinocytes between ECM_LW and Ctrl_LW. (A) Subclustering of fibroblasts showing 8 subsets; hierarchical clustering of average gene expression using pearson

correlation analysis. (B) Marker genes for each fibroblasts subset. (C) Proportion of each fibroblast subset in two groups. (D) GO enrichment analysis of wound fibroblast subtypes. (E) Subclustering of keratinocytes showing 10 subsets; hierarchical clustering of average gene expression using pearson correlation analysis. (F) Proportion of each keratinocytes subset in two groups. (G) Marker genes for each keratinocytes subset.

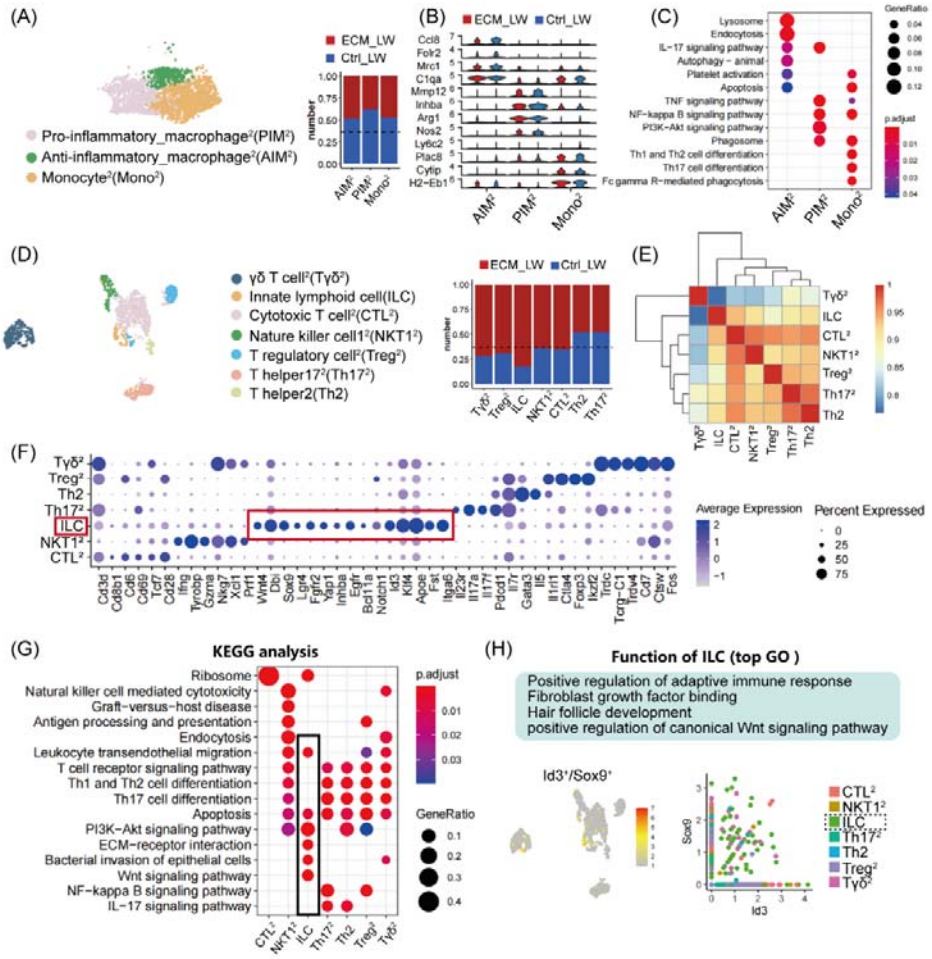

Fig. 8. Analysis of immune cells between ECM_LW and Ctrl_LW. (A) Subclustering of MAC showing three subsets and the composition for each subset. (B) Marker genes for each MAC subset and (C) enrichment analysis in KEGG pathway. (D) Subclustering of T cells showing seven subsets and the composition for each subset. (E) Pearson correlation analysis of T cell subsets based on average gene expression. (F) Marker genes for T cell subsets and (G) enrichment analysis of KEGG pathway.

(H) GO enrichment analysis of ILC; Overlay of Id3 and Sox9 expression onto the t-SNE space reveals $Id3^{+}$/ $Sox9^{+}$ double-positive subclusters

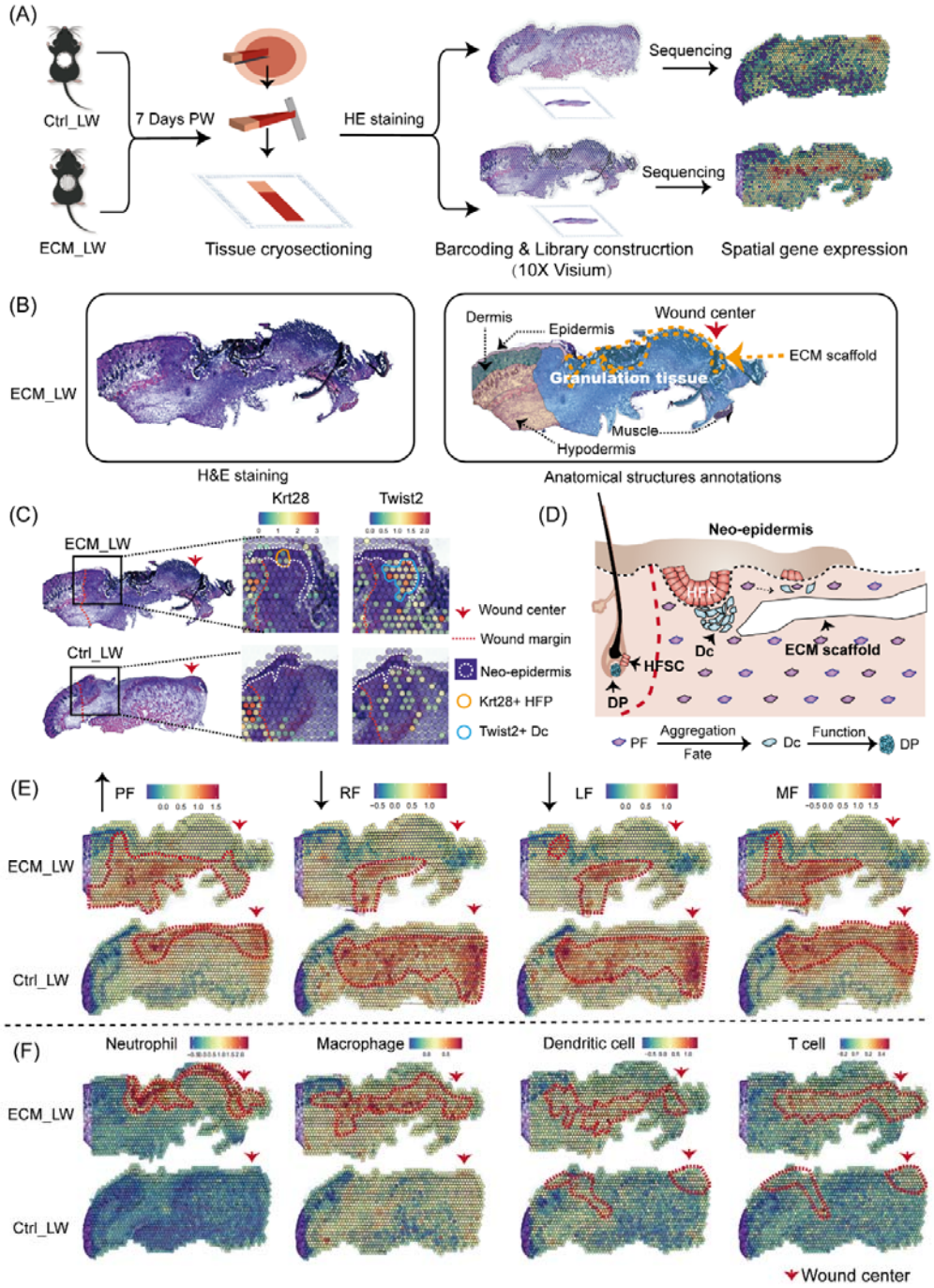

Fig.9. Spatial transcriptomics applied to ECM_LW and Ctrl_LW. (A) Schematic for generating spatial transcriptomics data from splinted excisional wounds. Fresh wound tissue was harvested, flash frozen,

embedded, and H&E staining. Each spot contained mRNA expression profiles of 1~10 cells. (B) The annotations indicated the anatomical structure of ECM_LW sample. (C) Spatial feature plot highlighted the expression of Krt28 and Twist2 in migrating neo-epidermis. (D) Illustration showed the epithelialization along with de novo HF formation in ECM_LW group. Spatial feature plots showed defined fibroblast subclusters (E) and immune cell (F) distribution in tissue sections using Addmodulescore.

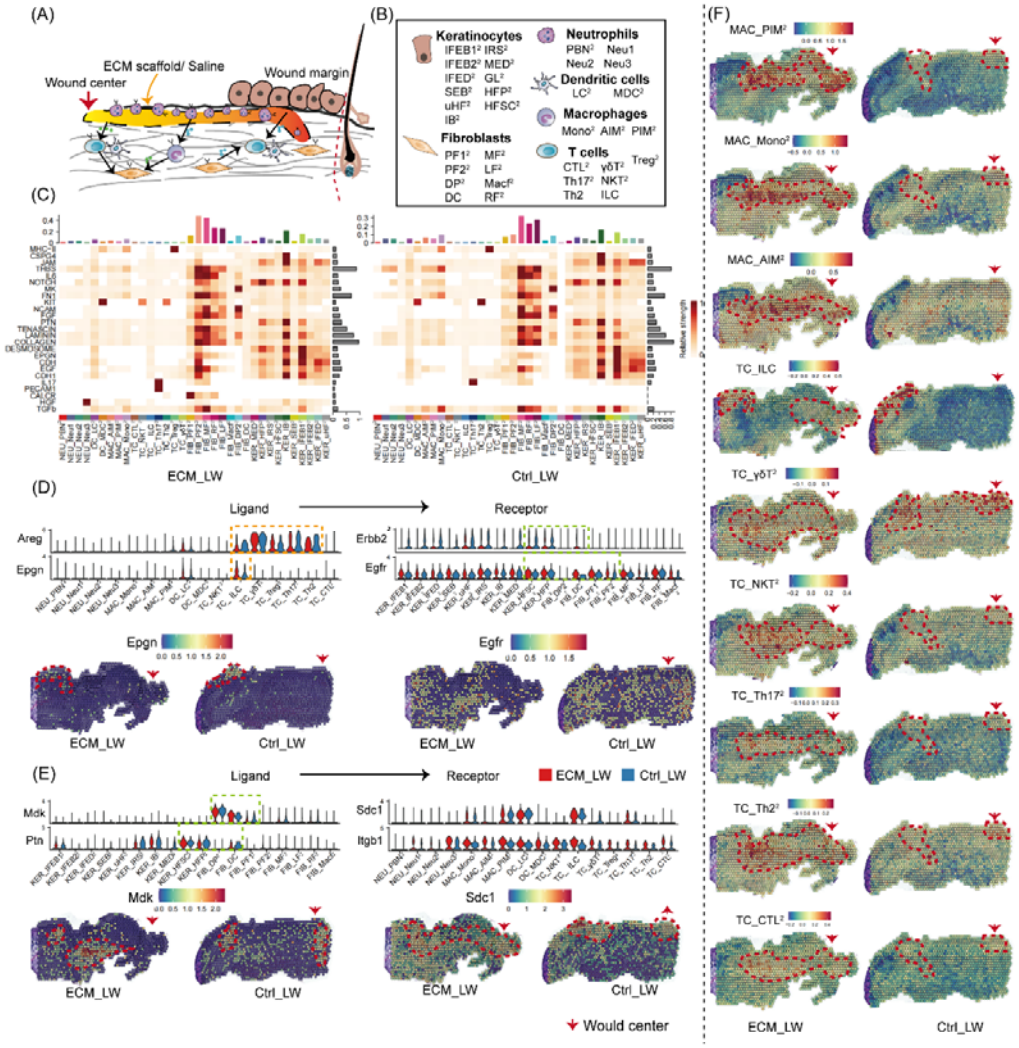

Fig.10. Cellular communication landscape between immune cells and cutaneous cells in ECM_LW and Ctrl_LW group. (A) Schematic of combined ligand-receptor analysis between keratinocytes, fibroblasts, and immune cells. (B) Defined subclusters in our scRNA-seq dataset. (C) Comparison of cell-cell communication patterns between ECM_LW and Ctrl_LW using CellChat. (D and E) Violin plot (scRNA-seq) and spatial feature plots (ST) showed select ligands and cognate receptor expression. (F) Spatial feature plots showed defined macrophages and T cells

subclusters distribution in tissue sections using Addmodulescore.

Materials and methods

Fabrication of biosynthetic ECM scaffolds

The preparation of biosynthetic ECM membranes was similar to our previous report[19].To fabricate the electrospinning scaffold with approximate 300nm diameter aligned fibers, 20% w/v PLGA (LA/GA = 75:25, molecular weight = 105 kDa, Jinan Daigang Biomaterial Co. Ltd.) and 2% w/v FC (Sangon Biotech Co. Ltd.) were dissolved in HFIP (Aladdin Co., Ltd.) with stirring until complete dissolution. The solution was fed at 0.018mm/min, and a voltage of -2/5kv and 11 cm distance between the needle (21G) and the rotating cylinder (2800 rpm) was applied. After been dried in a vacuum oven for a week, The morphology of PLGA/FC nanofibrous scaffold was observed by the scanning electron microscopy (SEM; JSM-7500F, JEOL, Japan). The scaffolds were cut into circular shape (0.8cm or 1.8cm in diameter) and sterilized using γ-irradiation before the animal implantation experiments.

Excisional wound model and implantation procedures

All procedures involving animals were approved by the Institution Review Board of West China Hospital of Stomatology (No. WCHSIRB-D-2017-033-R1). Female and male C57BL/6J mice (Dossy Experimental Animals Co., Ltd.), at the age of 6 week (~20 g) were used in this research. The large (1.5cm in diameter) and small (0.6cm in diameter) full-thickness skin wound were created in the mice dorsal skin. The mice

in this study were divided into four groups: small wounds transplanted with saline (Ctrl_SW) or biosynthetic ECM scaffolds below the wound (ECM_SW), and large wound transplanted with saline (Ctrl_LW) or biosynthetic ECM scaffolds below the wound (ECM_LW). Subsequently, the wounds were covered with sterile Tegaderm film (3M) and respectively fixed on the small (inner diameter 8 mm and outer diameter 12 mm, for small wound) or large (inner diameter 18 mm and outer diameter 22 mm, for large wound) silicone ring with uniform suture. Mice were euthanatized at 1, 2, and 4 weeks after the surgery, and the small (diameter 10 mm, for small wound) or large (diameter 25 mm, for large wound) round full-thickness sample was harvested.

Bulk RNA sequencing

Three replicates of mice skin wounds in each group were collected for the of Bulk RNA sequencing procedure. Total amounts and integrity of RNA were assessed using the RNA Nano 6000 Assay Kit of the Bioanalyzer 2100 system (Agilent Technologies, CA, USA). mRNA was purified from total RNA by using poly-T oligo-attached magnetic beads. The library fragments were purified with AMPure XP system (Beckman Coulter, Beverly, USA). The PCR amplification product was purified by AMPure XP beads. After the library is qualified by qRT-PCR, the different libraries are pooling and being sequenced by the Illumina NovaSeq 6000. FeatureCounts (v1.5.0-p3) was used to count the reads numbers mapped

to each gene. And then FPKM of each gene was calculated based on the length of the gene and reads count mapped to this gene. Differential expression analysis of two groups (three biological replicates per group) was performed using the DESeq2 R package (1.20.0), p−value <0.05 and $|\log_2(\text{foldchange})| > 1$ was set as the threshold for significantly differential expression. GO terms and KEGG pathways with corrected P-value less than 0.05 were considered significantly enriched by differential expressed genes.

Single cell RNA sequencing

Specimen harvest procedure for scRNA-seq was like our previous report[18],3~4 fresh samples were collected per group. In brief, the wound tissues were firstly digested by the Epidermis Dissociation Kit (Epidermis Dissociation Kit, mouse; Miltenyi Biotec) for enzymatic epidermal-dermal separation. The epidermis part was dissociated by a gentleMACS Dissociator (Miltenyi), then filtered (70-mm cell strainer, Corning, Durham), centrifuged (300g, 10 min, 4°C), and resuspended with phosphate-buffered saline (PBS) containing 0.5% bovine serum albumin (BSA). The dermis part was cut into 1 mm width pieces and mixed with mixed enzyme solution containing type I collagenase (Gibco, Grand Island) and trypsin (Gibco, Canada), then dissociated by gentleMACS Dissociator (Miltenyi), and digested for 2.5 hours in a hybridization oven (Peqlab PerfectBlot). After being dissociated, filtered, centrifuged, and

resuspended in red blood cell lysis buffer (Solarbio), the dermis cells were mixed with epidermis part. Then the dead cells and debris were removed by Dead Cell Removal MicroBeads (Miltenyi). Lastly, these suspensions were then carried out for Single-Cell RNA-seq (10x Genomics Chromium Single Cell Kit). Sequencing (10x Genomics Chromium Single Cell 3′ v3) was performed using an Illumina 1.9 mode. Then, reads were aligned, and expression matrices were generated for downstream analysis (Cell Ranger pipeline software). Filtering, normalization, scaling and canonical correlation analysis were performed (Seurat 4.1.2.) for integrated datasets. CellChat was used to predict receptor-ligand probability among cell subpopulations.

Spatial Transcriptomics

Fresh samples were rapidly harvested and frozen in OCT. Wound tissues were cryosectioned at -20 degrees onto gene expression slides. Tissue sections on the Capture Areas of the Visium Spatial Gene Expression are fixed using methanol, H&E staining images will be used downstream to map the gene expression patterns. Using the Visium Tissue Optimization Slide & Reagent kit, permeabilization time was optimized. Second Strand Mix is added to the tissue sections to initiate second strand synthesis. After transfer of cDNA from the slide, spatially barcoded, full-length cDNA is amplified via PCR to generate sufficient mass for library construction. The final libraries contain the P5 and P7 primers used in

Illumina amplification. A Visium Spatial Gene Expression library comprises standard Illumina paired-end constructs which begin and end with P5 and P7.

Raw FASTQ files and histology images were processed (SpaceRanger software) for genome alignment. Raw output files for each group were read into R studio (Seurat 4.1.2). Normalization across spots was performed with the SCTransform function. The spatial cluster gene signature overlap correlation matrix was generated by first taking all genes differentially expressed (avg_log2FC > 1 and adjusted p value < 0.05) across all ST clusters. Pearson correlation was calculated across this matrix and hierarchical clustering of ST clusters was performed with the heatmap function with the ggplots package. Signature scoring derived from scRNA-seq and ST signatures was performed with the AddModuleScore function.

Histopathology, Immunohistochemistry, and immunofluorescence microscopy

The samples were fixed with 4% paraformaldehyde at least 48 hours before ethanol and xylene dehydration. H&E staining and Masson's trichrome staining were performed for the observation of re-epithelialization and collagen fiber deposition. Immunofluorescence staining for cytokeratin 5 (ab52635, Abcam, 1:200) and cytokeratin 10 (ab76318, Abcam, 1:150) and was performed for to assess keratinization.

Immunofluorescence and immunofluorescence staining for Cd3 (GB13014, Servicebio, 1:100) and Cd68(GB11067, Servicebio, 1:100) was performed for the quantification the infiltration of T cells and macrophages.

Statistics and reproducibility

At least three independent replicates were conducted to obtain repeatable data, and the data was dealt with Case Viewer software, Image J software, and Prism 8.0 software. Statistical analyses were performed by Student's t-test or one-way analysis of variance (ANOVA) with Tukey post-hoc test. The numerical data are presented as mean ± standard deviation. A value of $p < 0.05$ was considered statistically significant (*$p < 0.05$, **$p < 0.01$, ***$p < 0.001$), and ns means no statistically significant difference.

CRediT authorship contribution statement

Yang Yang: Formal analysis, Investigation, Validation, Writing original draft, Resources. **Chenyu Chu:** Project administration, Methodology, Writing – review & editing. **Chen Hu**: Data curation. **Chenbing Wang:** Software, Data curation. **Yili Qu:** Funding acquisition, Supervision. **Yi Man**: Project administration, Funding acquisition.

Declaration of competing interest

The authors state no conflict of interest.

Acknowledgments

This work was supported by Key R & D Projects of Sichuan Science and Technology Plan (2022YFS0041), Interdisciplinary Innovation Project, West China Hospital of Stomatology Sichuan University (RD-03-202006), and Research and Develop Program, West China Hospital of Stomatology Sichuan University (No. LCYJ2019-19). We would like to thank the Novogene company for RNA sequencing work, thank the National Clinical Research Center for Oral Diseases & State Key Laboratory of Oral Diseases for sample harvest and Histological analysis, and thank the Analytical & Testing Center of Sichuan University for the fabrication of biosynthetic ECM scaffolds. We would like to thank Shengan Rung for the help with histological analysis.

Abbreviations:

HF: Hair follicle

WIHN: Wound-induced hair follicle neogenesis

scRNA-seq: Single-cell RNA sequencing

ST: Spatial transcriptomic

PIM: Pro-inflammatory macrophage

FBR: Foreign body reaction

ECM: Extracellular matrix

Bulk-seq: Bulk-tissue RNA sequencing

GO: Gene Ontology

KEGG: Kyoto Encyclopedia of Genes and Genomes

IF: Immunofluorescent

IHC: Immunohistochemistry

DP: dermal papilla

PF: Papillary fibroblast

RF: Reticular fibroblasts

LF: Lipo-fibroblast

Macf: Myeloid-derived adipocyte progenitors

HFSC: Hair follicle stem cell

HFP: Hair follicle progenitor

GL: Germinative layer

MED: Medulla

IRS: Inner root sheath

TAT: Telogen–anagen transition

MAC: Monocyte and macrophage

AIM: Anti-inflammatory macrophages

Mono: Monocyte

CTL: Cytotoxic T cell

NKT: Nature killer T cell

Th17: T helper17

Treg: T regulatory cell

UMAP: Uniform manifold approximation and projection

Krt5: Cytokeratin 5

Krt10: Cytokeratin 10

Dc: Dermal condensate

IFEB: Interfollicular epidermal basal cell

IFED: Interfollicular epidermal differentiated cell

PBN: Peripheral blood neutrophil

DC: Dendritic cell

LC: Langerhans cell

MDC: Monocyte derived dendritic cell

ILC: Innate lymphoid cell

Th2: T helper2

FBGC: Foreign body giant cell

EGF: Epidermal growth factor

EGFR: Epidermal growth factor receptor

EPGN: Epithelial mitogen

MDK: Midkine

PTN: Pleiotrophin

H&E: Haematoxylin and eosin

PLGA: Poly (lactic-co-glycolic acid)

FC: Fish collagen

HFIP: 1,1,1,3,3,3- Hexafluoro-2-propanol

NHS: N-hydroxysuccinimide

EDC: 1- ethyl-3-(3-dimehylaminopropyl) carbodiimide hydrochloride

SEM: Scanning electron microscopy

MST: Masson's trichrome

ANOVA: Analysis of variance

PBS: Phosphate-buffered saline

BSA: Bovine serum albumin

POD: Postoperative days

Reference

[1] Mascharak S, Desjardins-Park H E, Davitt M F, et al.Preventing Engrailed-1 activation in fibroblasts yields wound regeneration without scarring[J].Science,2021, 372 (6540).

[2] Willyard C.Unlocking the secrets of scar-free skin healing[J].Nature,2018, 563 (7732): S86-s88.

[3] Henn D, Chen K, Fehlmann T, et al.Xenogeneic skin transplantation promotes angiogenesis and tissue regeneration through activated Trem2(+) macrophages[J].Sci Adv,2021, 7 (49): eabi4528.

[4] Kurita M, Araoka T, Hishida T, et al.In vivo reprogramming of wound-resident cells generates skin epithelial tissue[J].Nature,2018, 561 (7722): 243-247.

[5] Ito M, Yang Z, Andl T, et al.Wnt-dependent de novo hair follicle regeneration in adult mouse skin after wounding[J].Nature,2007, 447 (7142): 316-20.

[6] Plikus M V, Guerrero-Juarez C F, Ito M, et al.Regeneration of fat cells from myofibroblasts during wound healing[J].Science,2017, 355 (6326): 748-752.

[7] Boothby I C, Cohen J N, Rosenblum M D.Regulatory T cells in skin injury: At the crossroads of tolerance and tissue repair[J].Sci Immunol,2020, 5 (47).

[8] Shook B A, Wasko R R, Rivera-Gonzalez G C, et al.Myofibroblast proliferation and heterogeneity are supported by macrophages during skin repair[J].Science,2018, 362 (6417).

[9] Gay D, Ghinatti G, Guerrero-Juarez C, et al.Phagocytosis of Wnt inhibitor SFRP4 by late wound macrophages drives chronic Wnt activity for fibrotic skin healing[J].Science advances,2020, 6 (12): eaay3704.

[10] Wang X, Chen H, Tian R, et al.Macrophages induce AKT/β-catenin-dependent Lgr5(+) stem cell activation and hair follicle regeneration through TNF[J].Nat Commun,2017, 8: 14091.

[11] Gay D, Kwon O, Zhang Z, et al.Fgf9 from dermal γδ T cells induces hair follicle neogenesis after wounding[J].Nat Med,2013, 19 (7): 916-23.

[12] Nelson A M, Katseff A S, Resnik S R, et al.Interleukin-6 Null Mice Paradoxically Display Increased STAT3 Activity and Wound-Induced Hair Neogenesis[J].J Invest Dermatol,2016, 136 (5): 1051-1053.

[13] Lee P, Gund R, Dutta A, et al.Stimulation of hair follicle stem cell proliferation through an IL-1 dependent activation of γδT-cells[J].Elife,2017, 6.

[14] Green J J, Elisseeff J H.Mimicking biological functionality with polymers for biomedical applications[J].Nature,2016, 540 (7633): 386-394.

[15] Yi B, Xu Q, Liu W.An overview of substrate stiffness guided cellular response and its applications in tissue regeneration[J].Bioactive Materials,2022, 15: 82-102.

[16] Sadtler K, Singh A, Wolf M T, et al.Design, clinical translation and immunological response of biomaterials in regenerative medicine[J].Nature Reviews Materials,2016, 1 (7): 16040.

[17] Griffin D, Archang M, Kuan C, et al.Activating an adaptive immune response from a hydrogel scaffold imparts regenerative wound healing[J].Nature materials,2021, 20 (4): 560-569.

[18] Hu C, Chu C, Liu L, et al.Dissecting the microenvironment around biosynthetic scaffolds in murine skin wound healing[J].Sci Adv,2021, 7 (22).

[19] Wang C, Chu C, Zhao X, et al.The diameter factor of aligned membranes facilitates wound healing by promoting epithelialization in an immune way[J].Bioact Mater,2022, 11: 206-217.

[20] Driskell R R, Lichtenberger B M, Hoste E, et al.Distinct fibroblast lineages determine dermal architecture in skin development and repair[J].Nature,2013, 504 (7479): 277-281.

[21] Foster D S, Januszyk M, Yost K E, et al.Integrated spatial multiomics reveals fibroblast fate during

tissue repair[J].Proc Natl Acad Sci U S A,2021, 118 (41).
[22] Phan Q M, Fine G M, Salz L, et al.Lef1 expression in fibroblasts maintains developmental potential in adult skin to regenerate wounds[J].Elife,2020, 9.
[23] Ma X, Tian Y, Song Y, et al.Msi2 Maintains Quiescent State of Hair Follicle Stem Cells by Directly Repressing the Hh Signaling Pathway[J].J Invest Dermatol,2017, 137 (5): 1015-1024.
[24] Morinaga H, Mohri Y, Grachtchouk M, et al.Obesity accelerates hair thinning by stem cell-centric converging mechanisms[J].Nature,2021, 595 (7866): 266-271.
[25] Abbasi S, Sinha S, Labit E, et al.Distinct Regulatory Programs Control the Latent Regenerative Potential of Dermal Fibroblasts during Wound Healing[J].Cell Stem Cell,2020, 27 (3): 396-412.e6.
[26] Guerrero-Juarez C F, Dedhia P H, Jin S, et al.Single-cell analysis reveals fibroblast heterogeneity and myeloid-derived adipocyte progenitors in murine skin wounds[J].Nat Commun,2019, 10 (1): 650.
[27] Shook B A, Wasko R R, Mano O, et al.Dermal Adipocyte Lipolysis and Myofibroblast Conversion Are Required for Efficient Skin Repair[J].Cell Stem Cell,2020, 26 (6): 880-895.e6.
[28] Joost S, Annusver K, Jacob T, et al.The Molecular Anatomy of Mouse Skin during Hair Growth and Rest[J].Cell Stem Cell,2020, 26 (3): 441-457.e7.
[29] Joost S, Zeisel A, Jacob T, et al.Single-Cell Transcriptomics Reveals that Differentiation and Spatial Signatures Shape Epidermal and Hair Follicle Heterogeneity[J].Cell Syst,2016, 3 (3): 221-237.e9.
[30] Rinkevich Y, Walmsley G G, Hu M S, et al.Skin fibrosis. Identification and isolation of a dermal lineage with intrinsic fibrogenic potential[J].Science,2015, 348 (6232): aaa2151.
[31] Telerman S B, Rognoni E, Sequeira I, et al.Dermal Blimp1 Acts Downstream of Epidermal TGFβ and Wnt/β-Catenin to Regulate Hair Follicle Formation and Growth[J].J Invest Dermatol,2017, 137 (11): 2270-2281.
[32] Haensel D, Jin S, Sun P, et al.Defining Epidermal Basal Cell States during Skin Homeostasis and Wound Healing Using Single-Cell Transcriptomics[J].Cell Rep,2020, 30 (11): 3932-3947.e6.
[33] Hughes M W, Jiang T X, Plikus M V, et al.Msx2 Supports Epidermal Competency during Wound-Induced Hair Follicle Neogenesis[J].J Invest Dermatol,2018, 138 (9): 2041-2050.
[34] Wynn T A, Vannella K M.Macrophages in Tissue Repair, Regeneration, and Fibrosis[J].Immunity,2016, 44 (3): 450-462.
[35] Sadtler K, Estrellas K, Allen B W, et al.Developing a pro-regenerative biomaterial scaffold microenvironment requires T helper 2 cells[J].Science,2016, 352 (6283): 366-70.
[36] Bassez A, Vos H, Van Dyck L, et al.A single-cell map of intratumoral changes during anti-PD1 treatment of patients with breast cancer[J].Nat Med,2021, 27 (5): 820-832.
[37] Qian B Z, Li J, Hui Z, et al.CCL2 recruits inflammatory monocytes to facilitate breast-tumour metastasis[J].Nature,2012, 475 (7355): 222-225.
[38] Aragona M, Dekoninck S, Rulands S, et al.Defining stem cell dynamics and migration during wound healing in mouse skin epidermis[J].Nat Commun,2017, 8: 14684.
[39] Park S, Gonzalez D G, Guirao B, et al.Tissue-scale coordination of cellular behaviour promotes epidermal wound repair in live mice[J].Nat Cell Biol,2017, 19 (2): 155-163.
[40] Ji A L, Rubin A J, Thrane K, et al.Multimodal Analysis of Composition and Spatial Architecture in Human Squamous Cell Carcinoma[J].Cell,2020, 182 (2): 497-514.e22.
[41] Almet A A, Cang Z, Jin S, et al.The landscape of cell-cell communication through single-cell transcriptomics[J].Curr Opin Syst Biol,2021, 26: 12-23.
[42] Jin S, Guerrero-Juarez C, Zhang L, et al.Inference and analysis of cell-cell communication using

CellChat[J].Nature communications,2021, 12 (1): 1088.
[43] Wang W, Hu C K, Zeng A, et al.Changes in regeneration-responsive enhancers shape regenerative capacities in vertebrates[J].Science,2020, 369 (6508).
[44] Seo C, Kwack M, Kim M, et al.Activin A-induced signalling controls hair follicle neogenesis[J].Experimental dermatology,2017, 26 (2): 108-115.
[45] Monavarian M, Kader S, Moeinzadeh S, et al.Regenerative Scar-Free Skin Wound Healing[J].Tissue Eng Part B Rev,2019, 25 (4): 294-311.
[46] Mok K, Saxena N, Heitman N, et al.Dermal Condensate Niche Fate Specification Occurs Prior to Formation and Is Placode Progenitor Dependent[J].Developmental cell,2019, 48 (1): 32-48.e5.
[47] Kim D, Chen R, Sheu M, et al.Noncoding dsRNA induces retinoic acid synthesis to stimulate hair follicle regeneration via TLR3[J].Nat Commun,2019, 10 (1): 2811.
[48] Ode Boni B O, Lamboni L, Souho T, et al.Immunomodulation and cellular response to biomaterials: the overriding role of neutrophils in healing[J].Materials Horizons,2019, 6 (6): 1122-1137.
[49] Riffelmacher T, Clarke A, Richter F C, et al.Autophagy-Dependent Generation of Free Fatty Acids Is Critical for Normal Neutrophil Differentiation[J].Immunity,2017, 47 (3): 466-480.e5.
[50] Chu C, Liu L, Rung S, et al.Modulation of foreign body reaction and macrophage phenotypes concerning microenvironment[J].J Biomed Mater Res A,2020, 108 (1): 127-135.
[51] Yu Y, Tsang J C, Wang C, et al.Single-cell RNA-seq identifies a PD-1(hi) ILC progenitor and defines its development pathway[J].Nature,2016, 539 (7627): 102-106.
[52] Bielecki P, Riesenfeld S J, Hütter J C, et al.Skin-resident innate lymphoid cells converge on a pathogenic effector state[J].Nature,2021, 592 (7852): 128-132.
[53] Shih H Y, Sciumè G, Mikami Y, et al.Developmental Acquisition of Regulomes Underlies Innate Lymphoid Cell Functionality[J].Cell,2016, 165 (5): 1120-1133.
[54] Li Z, Hodgkinson T, Gothard E J, et al.Epidermal Notch1 recruits RORγ(+) group 3 innate lymphoid cells to orchestrate normal skin repair[J].Nat Commun,2016, 7: 11394.
[55] Ebbo M, Crinier A, Vély F, et al.Innate lymphoid cells: major players in inflammatory diseases[J].Nat Rev Immunol,2017, 17 (11): 665-678.
[56] Chang D T, Colton E, Anderson J M.Paracrine and juxtacrine lymphocyte enhancement of adherent macrophage and foreign body giant cell activation[J].J Biomed Mater Res A,2009, 89 (2): 490-8.
[57] Saxena N, Mok K W, Rendl M.An updated classification of hair follicle morphogenesis[J].Exp Dermatol,2019, 28 (4): 332-344.
[58] Ali N, Zirak B, Rodriguez R S, et al.Regulatory T Cells in Skin Facilitate Epithelial Stem Cell Differentiation[J].Cell,2017, 169 (6): 1119-1129.e11.
[59] Nosbaum A, Prevel N, Truong H A, et al.Cutting Edge: Regulatory T Cells Facilitate Cutaneous Wound Healing[J].J Immunol,2016, 196 (5): 2010-4.
[60] Thulabandu V, Chen D, Atit R P.Dermal fibroblast in cutaneous development and healing[J].Wiley Interdiscip Rev Dev Biol,2018, 7 (2).
[61] Wang G, Sweren E, Liu H, et al.Bacteria induce skin regeneration via IL-1β signaling[J].Cell Host Microbe,2021, 29 (5): 777-791.e6.
[62] Ge Y, Fuchs E.Stretching the limits: from homeostasis to stem cell plasticity in wound healing and cancer[J].Nature Reviews Genetics,2018, 19 (5): 311-325.
[63] Chu S Y, Chou C H, Huang H D, et al.Mechanical stretch induces hair regeneration through the alternative activation of macrophages[J].Nat Commun,2019, 10 (1): 1524.

[64] Yuriguchi M, Aoki H, Taguchi N, et al.Pigmentation of regenerated hairs after wounding[J].J Dermatol Sci,2016, 84 (1): 80-87.

Supplementary files:

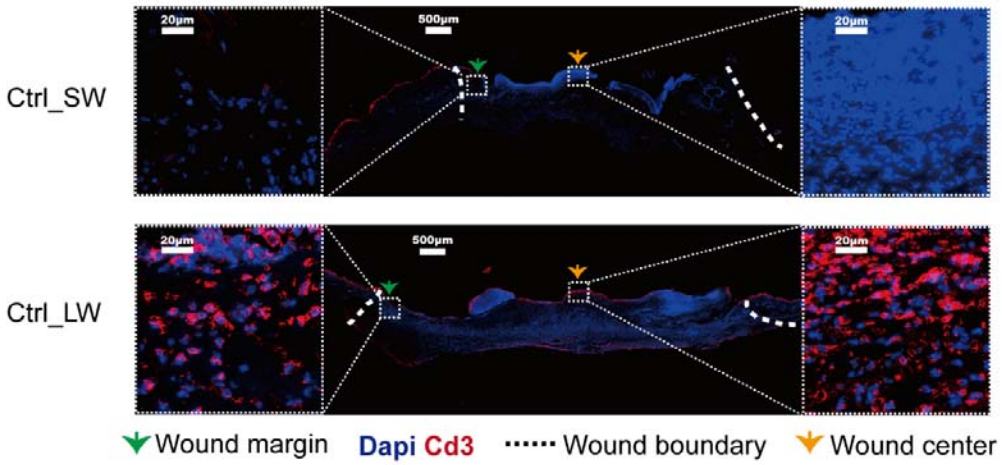

Fig.S1. IF staining of Cd3^{+}T cell in Ctrl_SW and Ctrl_LW on POD7.

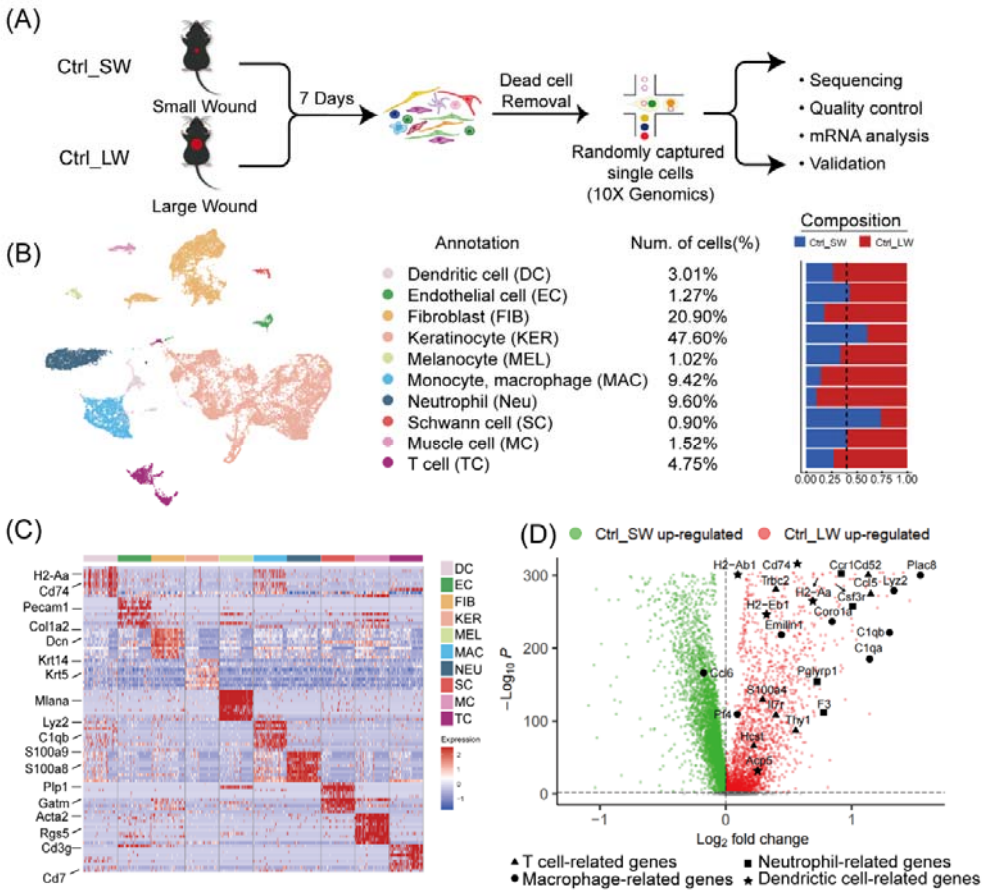

Fig.S2. Overview of the single-cell transcriptome analysis between Ctrl_SW and Ctrl_LW. (A) Single-cell experiment workflow. (B) Cells were categorized into 10 main clusters. The number of cell populations in each cluster, number of cells (%), and composition of Ctrl_SW and Ctrl_LW groups were listed. (C) Heatmap showed top10 marker genes for different clusters. (D) Volcano plot showing interested differentially expressed genes in Ctrl_SW and Ctrl_LW group (Sc-RNA).

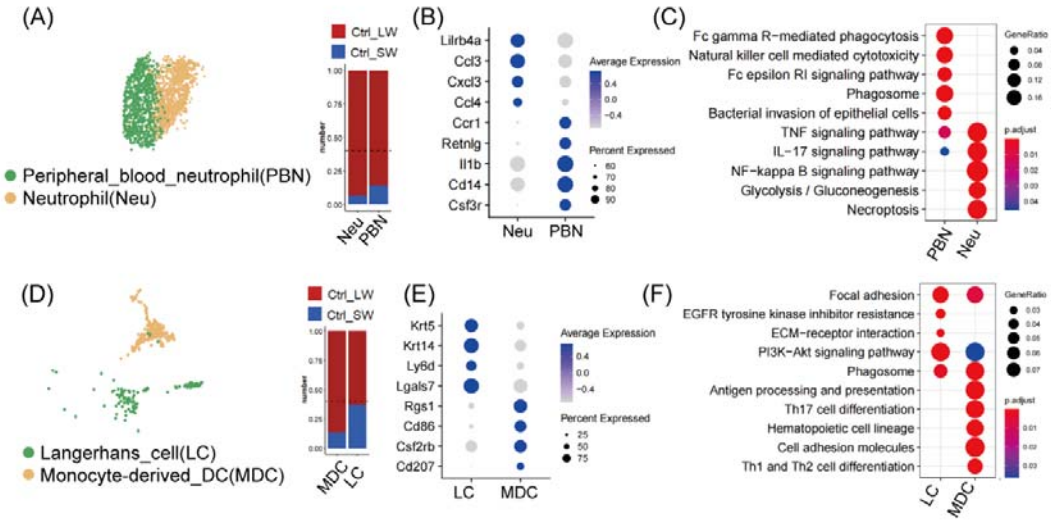

Fig.S3. Further scRNA-seq analysis of neutrophils and dendritic cells between Ctrl_SW and Ctrl_LW. (A) Subclustering of neutrophils showing 2 subsets and the composition for each subset. (B) Marker genes for each neutrophil subset. (C) Gene enrichment analysis of KEGG pathway. (D) Subclustering of dendritic cells showing two subsets and the composition for each subset. (E) Marker genes for each dendritic cell subset. (F) Gene enrichment analysis of KEGG pathway.

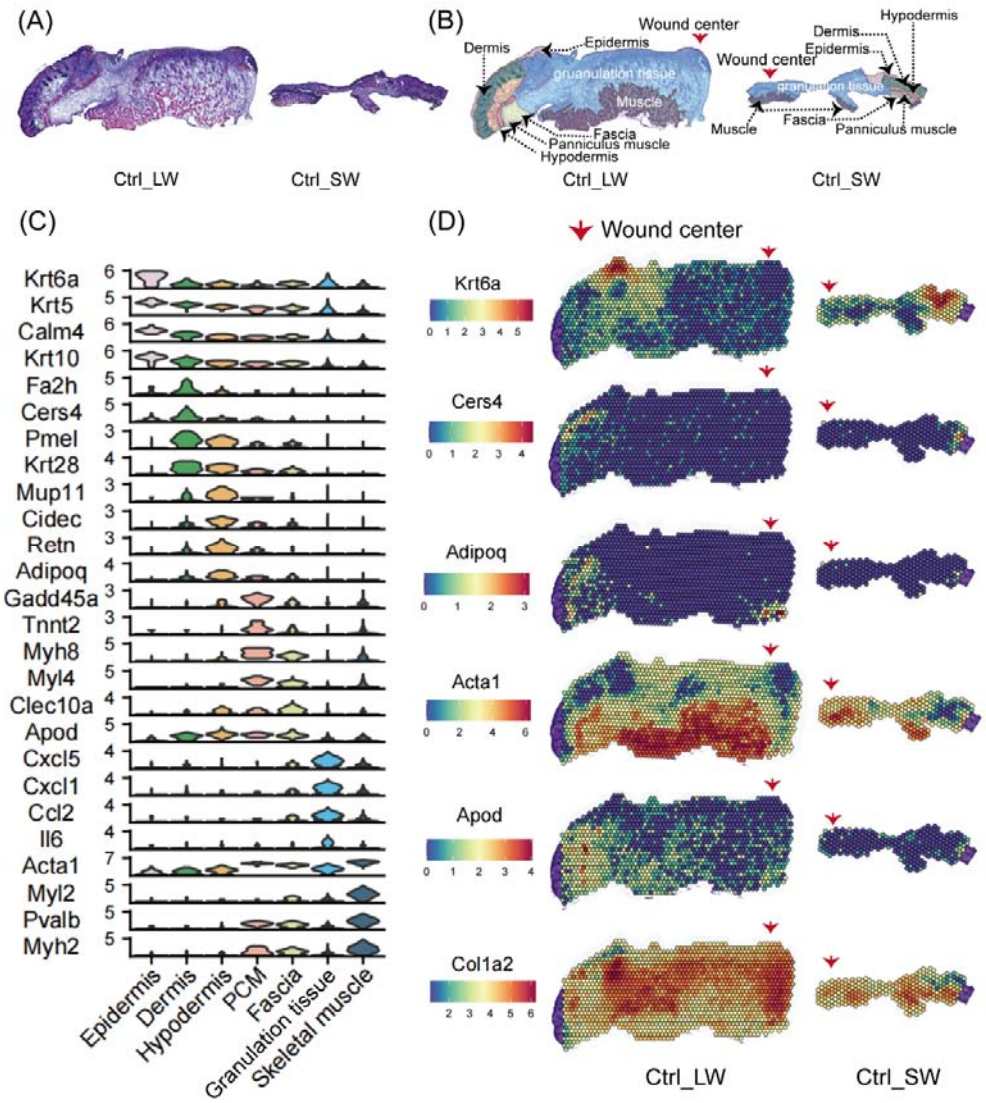

Fig.S4. Spatial transcriptomics profiles of Ctrl_SW and Ctrl_LW. (A) Original histological images with H&E staining. (B) Annotations indicated the anatomical structures. (C) Stacked violin plot showed marker genes differentially expressed in each region. (D) Spatial feature plot showed representative marker gene of each region.

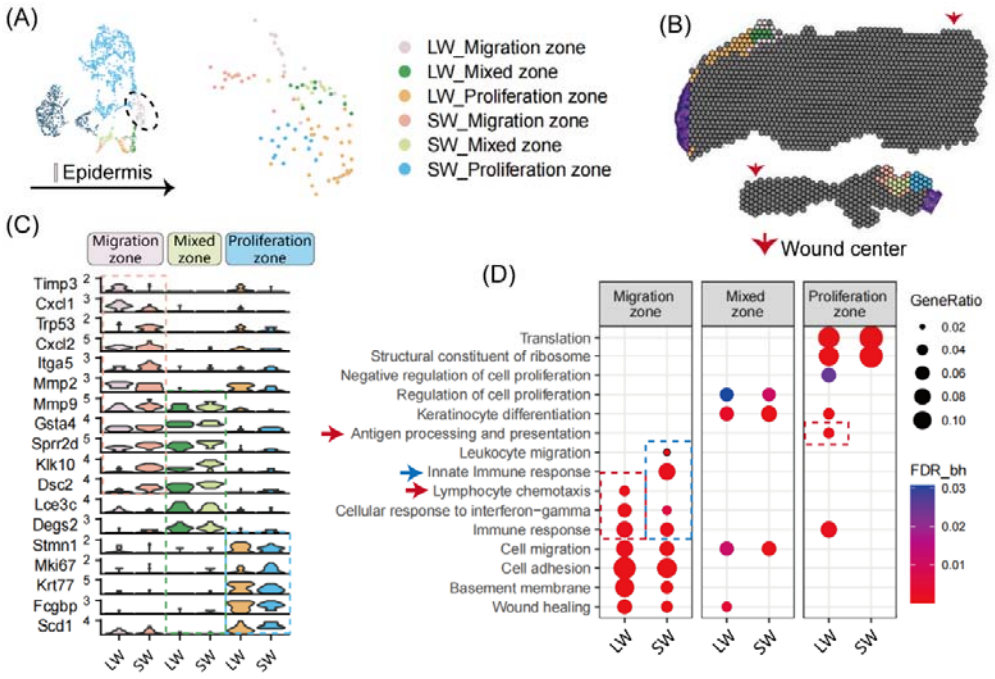

Fig.S5. Further subclustering analysis of epidermis in Ctrl_SW and Ctrl_LW. (A)Subsets of epidermis in each group. (B) Corresponding spatial plot. (C) StackedVlnPlot showed marker genes differentially expressed in each region. (D) Enrichment analysis of GO terms.

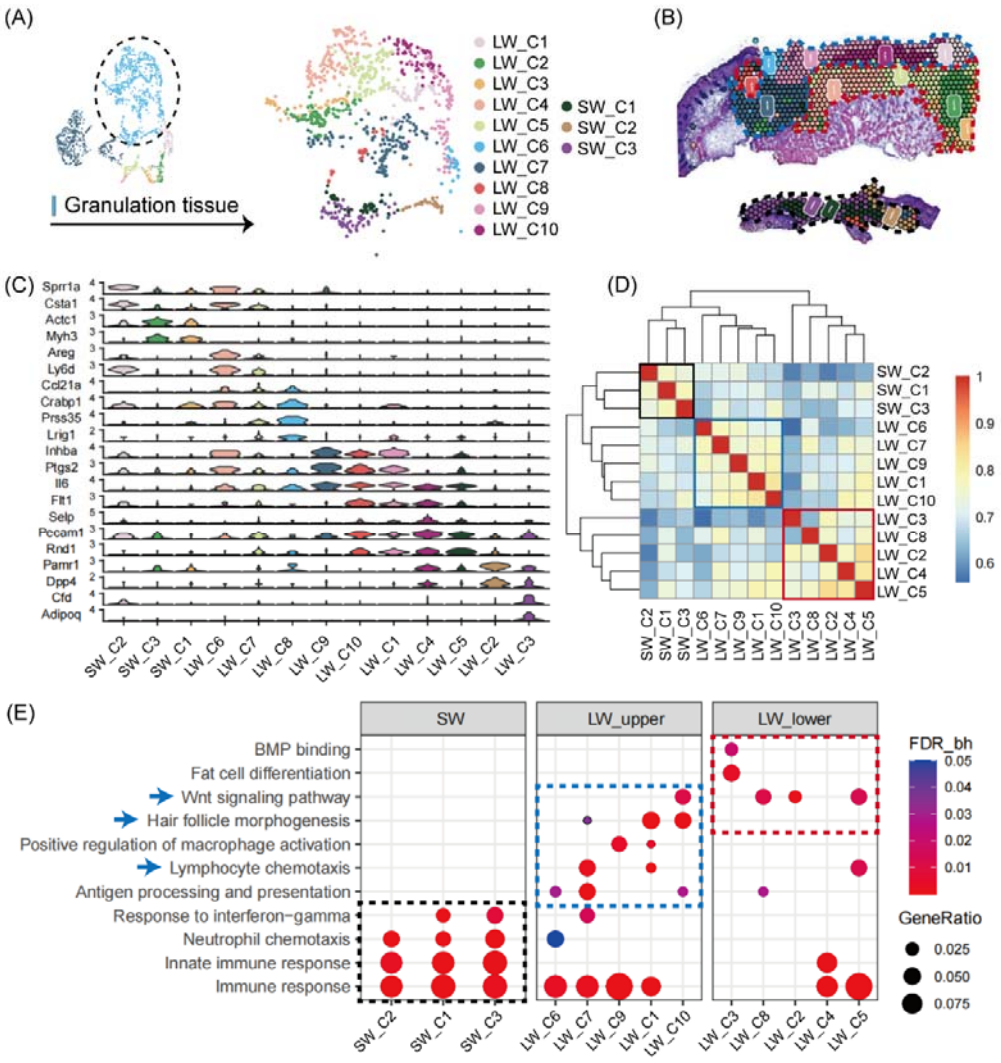

Fig.S6. Further subclustering analysis of granulation tissue in Ctrl_SW and Ctrl_LW. (A) Subsets of granulation tissue in each group. (B) Corresponding spatial plot of each region. (C) StackedVlnPlot showed marker genes differentially expressed in each region. (D) 13 regions were grouped into three functional clusters by pearson correlation analysis. (E) Enrichment analysis of GO terms.

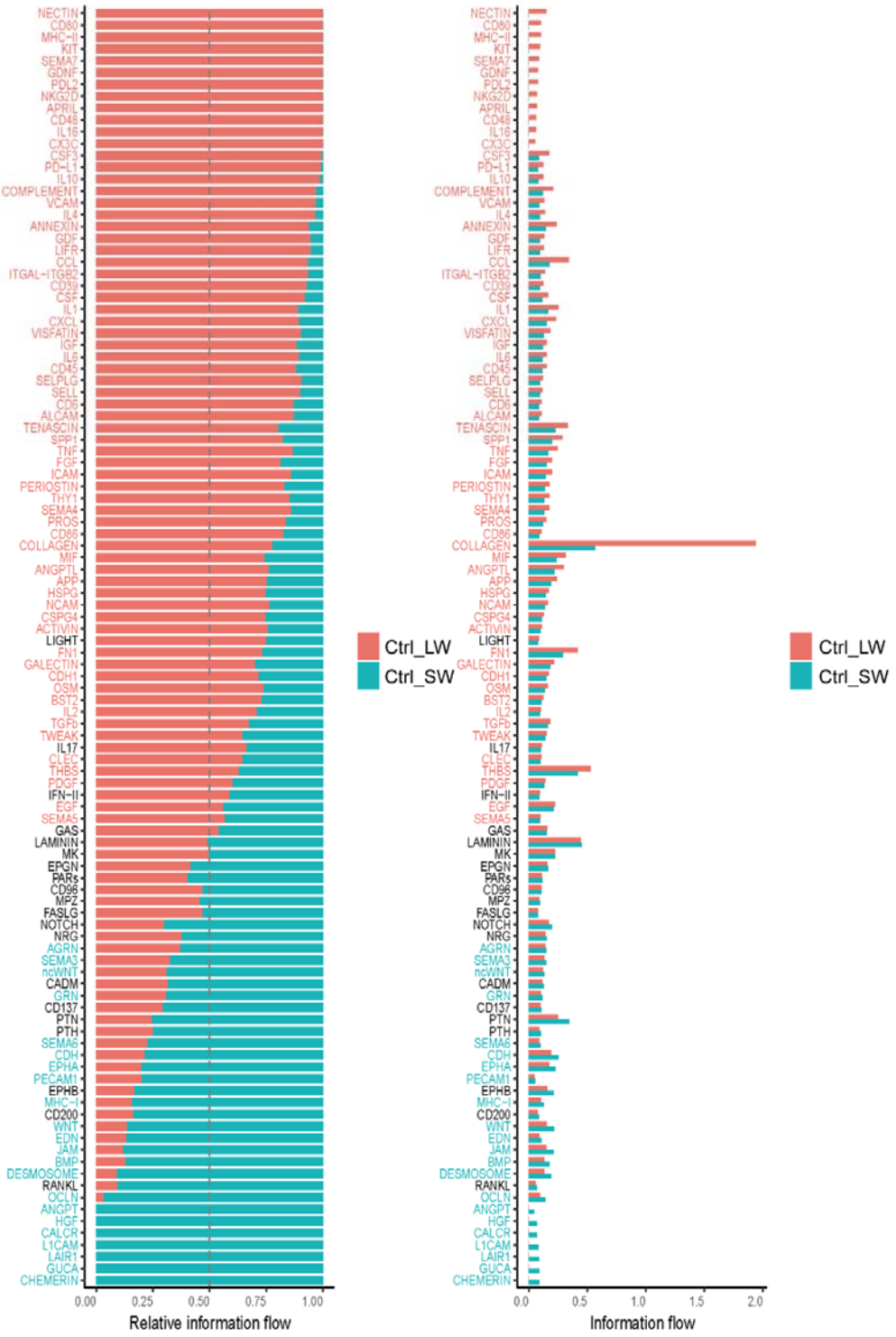

Fig.S7. Comparison of the overall information flow between Ctrl_SW and Ctrl_LW. Bar graph showed significant signaling pathways which

were ranked based on differences in the overall information flow between Ctrl_SW and Ctrl_LW. The top signaling pathways colored red were enriched in Ctrl_LW, and these colored green were enriched in the Ctrl_SW group.

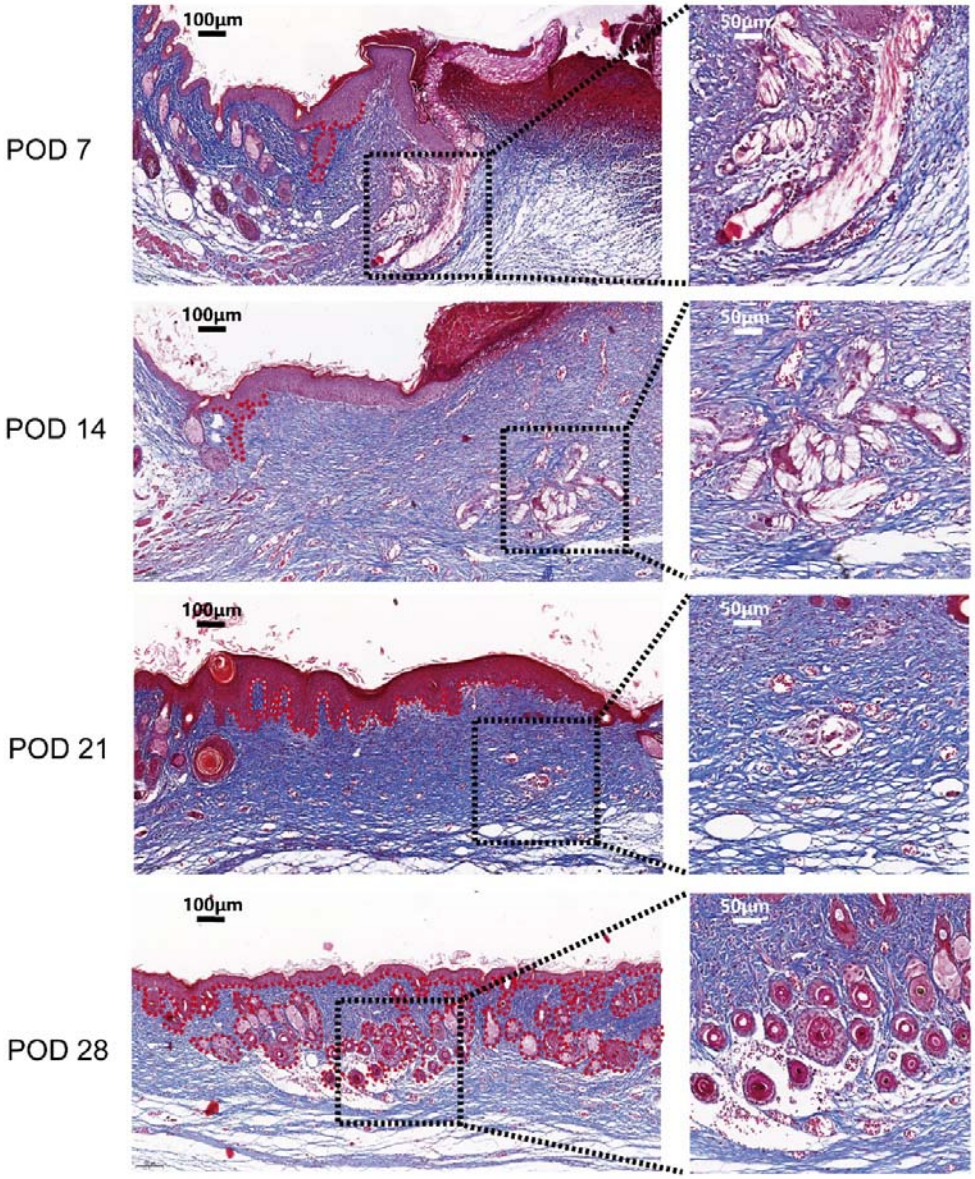

Fig.S8. Evaluation of FBR around the biomaterials. MST staining for ECM_LW group on POD 7, 14, 21 and 28.

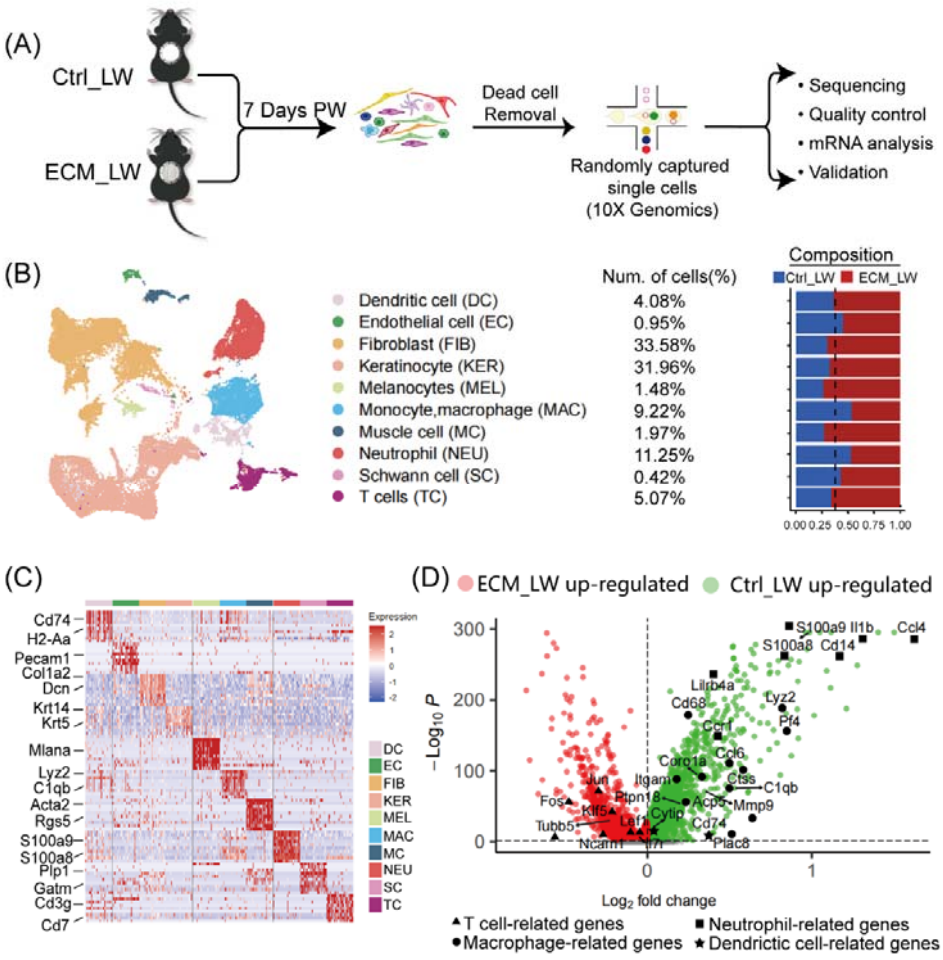

Fig.S9. Overview of the single-cell transcriptome analysis between ECM_LW and Ctrl_LW. (A) Single-cell experiment workflow. (B) Cells were categorized into 10 main clusters. The number of cell populations in each cluster, number of cells (%), and composition of ECM_LW and Ctrl_LW groups were listed. (C) Heatmap showed top10 marker genes for each cluster. (D) Volcano plot showing interested differentially expressed genes in ECM_LW and Ctrl_LW group (scRNA-seq).

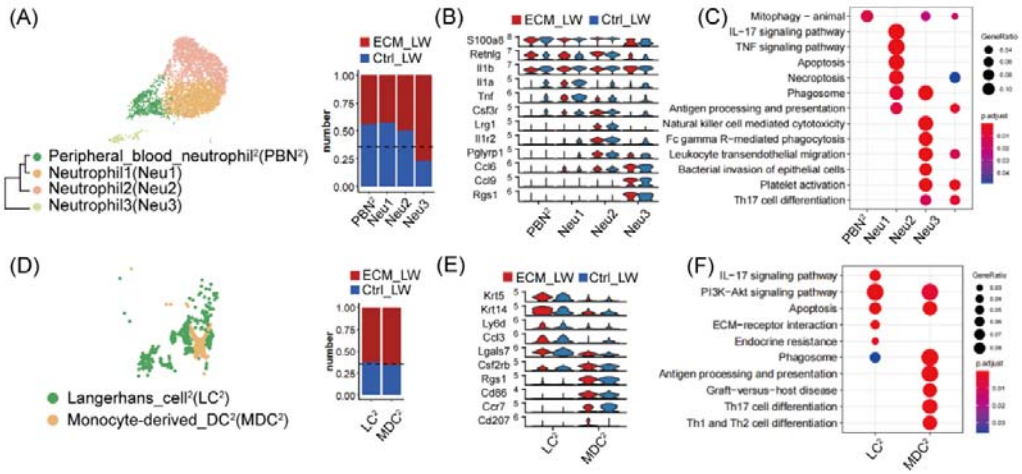

Fig.S10. Subclustering analysis of neutrophils and dendritic cells between ECM_LW and Ctrl_LW. (A) Subclustering of neutrophils showing 4 subsets and hierarchical clustering of average gene expression using pearson correlation analysis. The composition for each subset was listed. (B) Marker genes for each neutrophil subset. (C) Gene enrichment analysis of KEGG pathway. (D) Subclustering of dendritic cells showing two subsets and the composition for each subset was listed. (E) Marker genes for each dendritic cells subset. (F) Gene enrichment analysis of KEGG pathway.

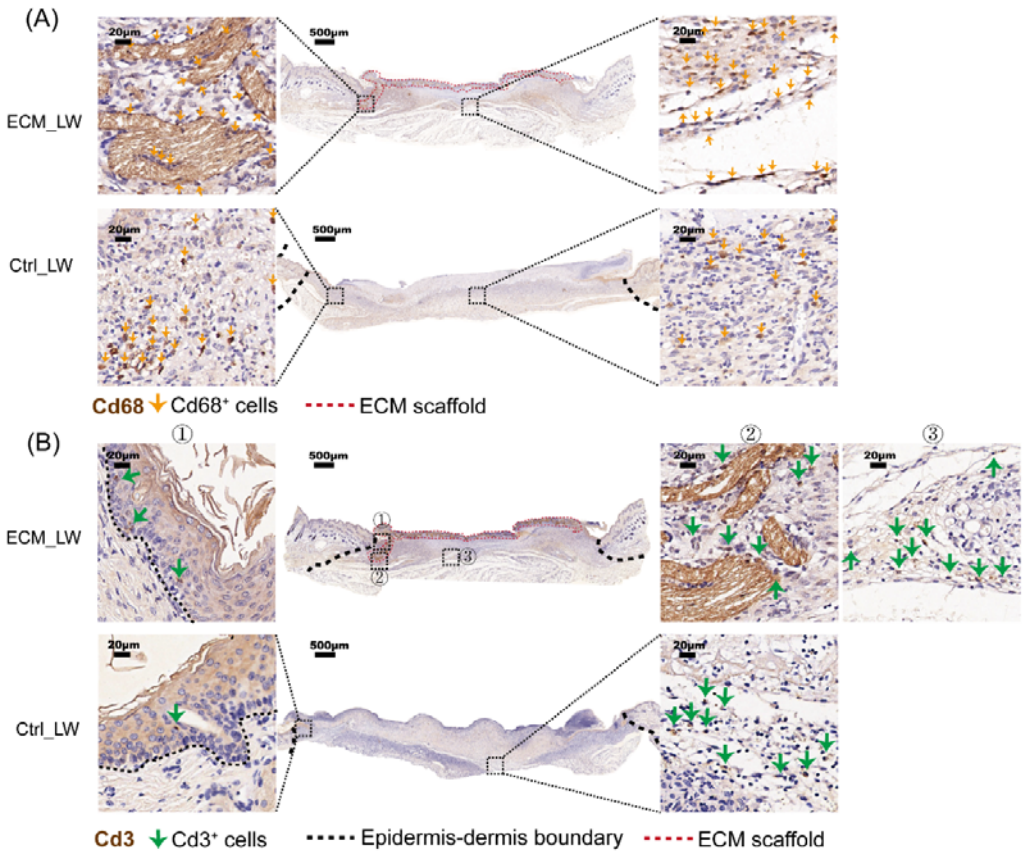

Fig.S11. IHC staining of (A) Cd68^{+} macrophage and (B) Cd3^{+} T cell in ECM_LW and Ctrl_LW on POD7.

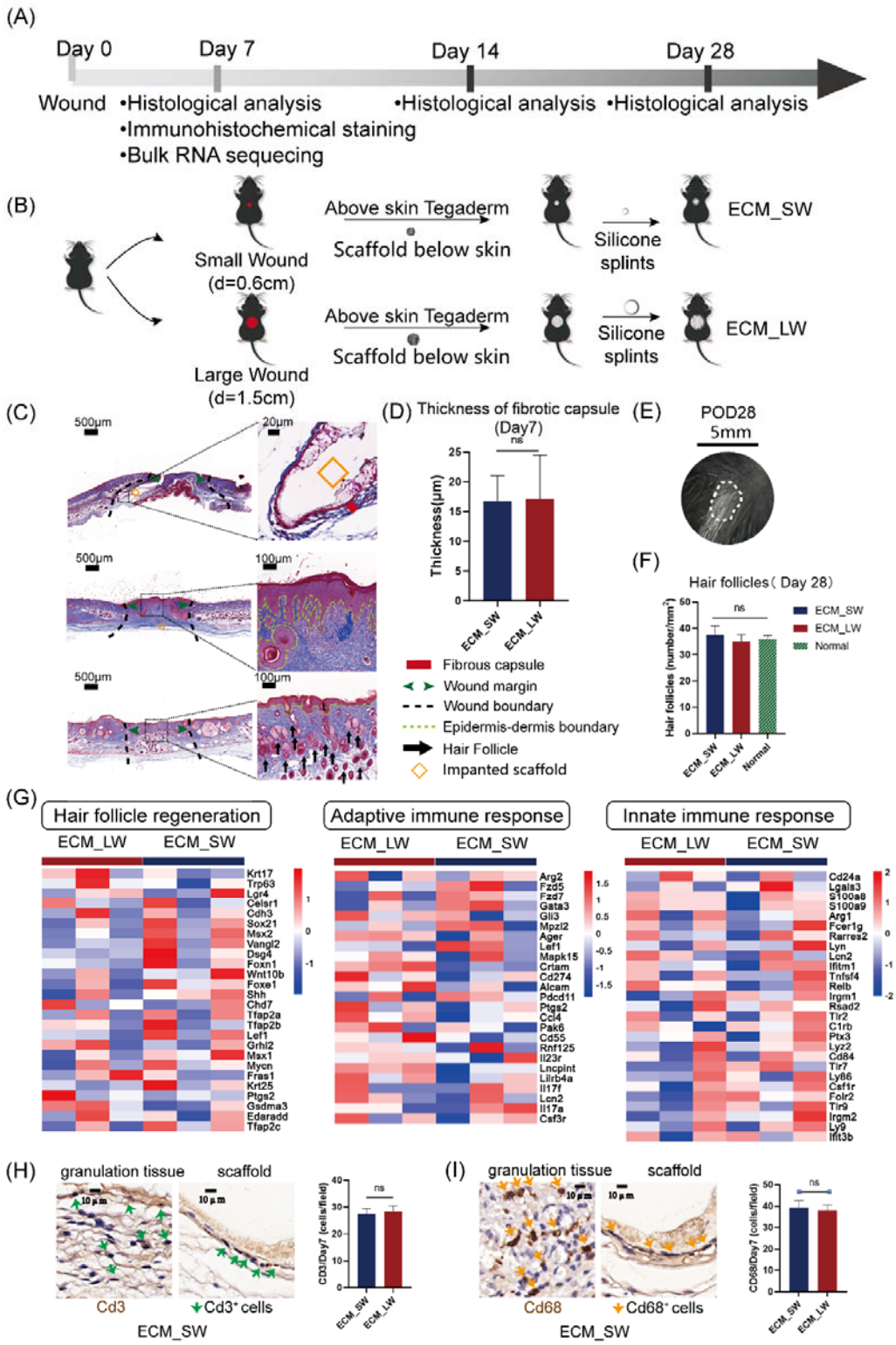

Fig.S12. Evaluation of the healing of small and large full-thickness wound with implanted ECM scaffolds. (A) Workflow for evaluating

skin wound healing. (B) Surgical process for skin excisional wound model of ECM_SW and ECM_LW group. (C) MST staining of ECM_SW samples. (D) Thickness of fibrotic capsule around membrane of ECM_SW and ECM_LW group. (E) Gross photograph of small wound treated with scaffold on POD28. (F) Histologic quantification of de novo hair follicles on POD28. (G) Heatmap showing expression of hair follicle regeneration, adaptive immune response, and innate immune response related genes. (H) IHC staining of Cd3 in ECM_SW sample and comparison of $CD3^+$ cellular infiltration between ECM_SW and ECM_LW. (I) IHC staining of Cd68 in ECM_SW sample and comparison of $CD68^+$ cellular infiltration between ECM_SW and ECM_LW.

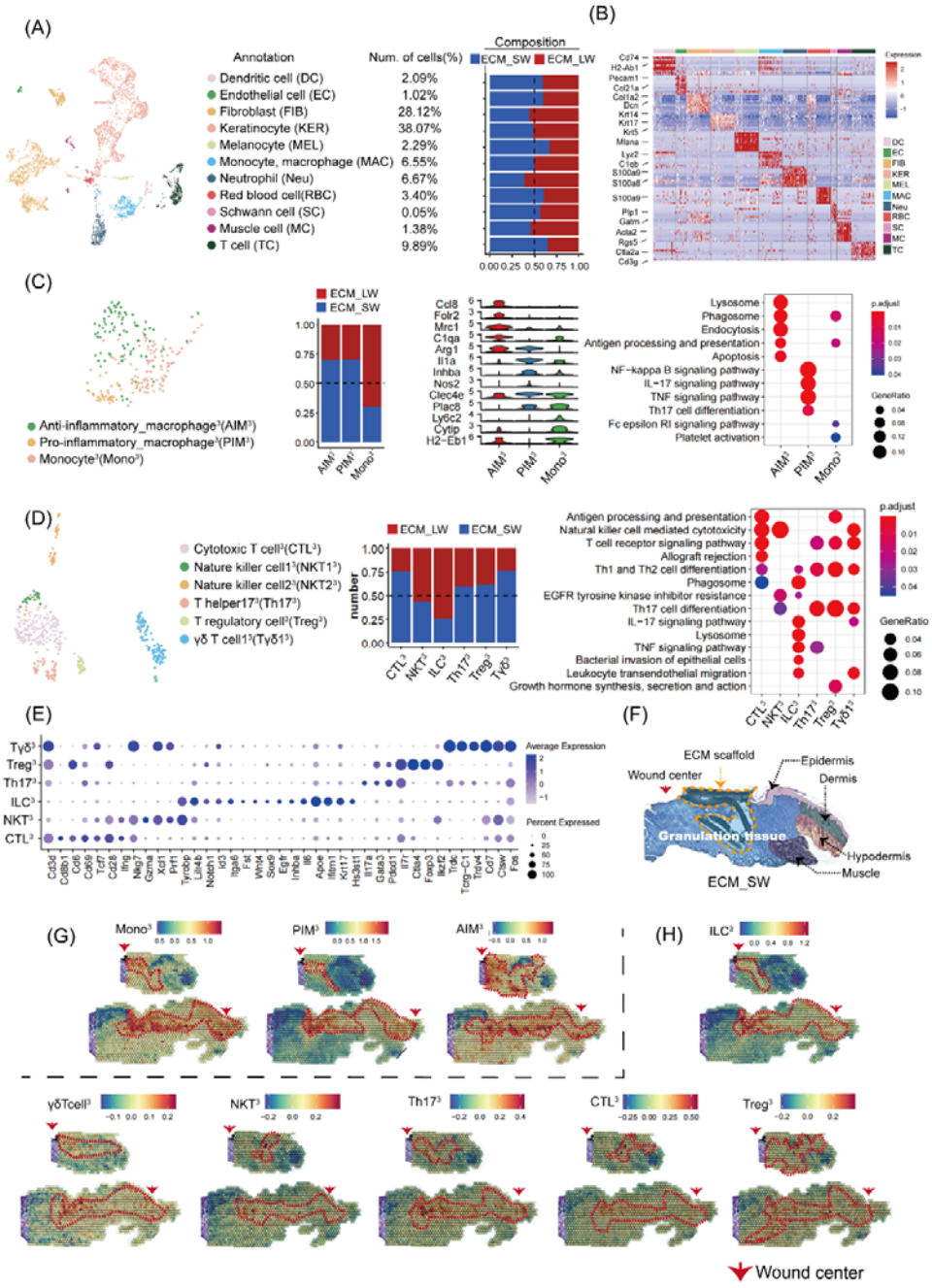

Fig.S13. ScRNA-seq and ST analysis between ECM_SW and ECM_LW. (A) Single cells were categorized into 11 main clusters. The number of cell populations in each cluster, number of cells (%), and composition of ECM_LW and ECM_SW groups were listed. Heatmap

and top10 marker genes for each cluster. (C) Subclustering of MAC showing three subsets; The composition for each subset was listed; Marker genes for each MAC subset and enrichment analysis of KEGG pathway. (D) Subclustering of T cells showing seven subsets; The composition for each subset was listed and enrichment analysis of KEGG analysis. (E) Marker genes for T cell subsets. (F) The annotations indicated the anatomical structures of ECM_SW sample. Spatial feature plots showed defined MAC (G) and T cells subclusters (H) distribution using Addmodulescore.